JOURNAL OF GEOPHYSICAL RESEARCH, VOL. 115, C07005, doi:10.1029/2009JC005750, 2010

Click Here for Full Article

Where and how long ago was water in the western North Atlantic ventilated? Maximum entropy inversions of bottle data from WOCE line A20

Mark Holzer,[1,2,3,4] François W. Primeau,[5] William M. Smethie Jr.,[6] and Samar Khatiwala[6]

Received 23 August 2009; revised 18 January 2010; accepted 15 February 2010; published 7 July 2010.

[1] A maximum entropy (ME) method is used to deconvolve tracer data for the joint distribution $\mathcal{G}$ of locations and times since last ventilation. The deconvolutions utilize World Ocean Circulation Experiment line A20 repeat hydrography for CFC-11, potential temperature, salinity, oxygen, and phosphate, as well as Global Ocean Data Analysis Project (GLODAP) radiocarbon data, combined with surface boundary conditions derived from the atmospheric history of CFC-11 and the World Ocean Atlas 2005 and GLODAP databases. Because of the limited number of available tracers the deconvolutions are highly underdetermined, leading to large entropic uncertainties, which are quantified using the information entropy of $\mathcal{G}$ relative to a prior distribution. Additional uncertainties resulting from data sparsity are estimated using a Monte Carlo approach and found to be of secondary importance. The ME deconvolutions objectively identify key water mass formation regions and quantify the local fraction of water of age τ or older last ventilated in each region. Ideal mean age and radiocarbon age are also estimated but found to have large entropic uncertainties that can be attributed to uncertainties in the partitioning of a given water parcel according to where it was last ventilated. Labrador/Irminger seawater (L water) is determined to be mostly less than ~40 a old in the vicinity of the deep western boundary current (DWBC) at the northern end of A20 but several decades older where the DWBC recrosses the section further south, pointing to the importance of mixing via a multitude of eddy-diffusive paths. Overflow water lies primarily below L water with young waters ($\tau \lesssim 40$ a) at middepth in the northern part of A20 and waters as old as ~600 a below ~3500 m.

Citation: Holzer, M., F. W. Primeau, W. M. Smethie Jr., and S. Khatiwala (2010), Where and how long ago was water in the western North Atlantic ventilated? Maximum entropy inversions of bottle data from WOCE line A20, *J. Geophys. Res.*, *115*, C07005, doi:10.1029/2009JC005750.

1. Introduction

[2] Water mass properties such as salinity, S, temperature, T, and the concentrations of tracers of atmospheric origin are determined in the mixed layer through the interplay of air-sea exchange processes and the ocean circulation. Similarly, the preformed component of nutrient tracers is by definition determined by the mixed layer concentration of the nutrients. Subsequent transport carries the water mass properties and preformed nutrients into the ocean interior. The local water mass properties and tracer concentrations at any point in the interior are then determined by the admixture of fluid elements of different surface origin and different transit times since last surface contact.

[3] We focus on the deep waters in the North Atlantic because of their importance in the ventilation and circulation of the global ocean. Numerous investigators have extensively studied the formation and circulation of these waters building a knowledge base that provides context and reference for our results from the maximum entropy inversions. North Atlantic Deep Water (NADW) forms from dense waters originating in the Arctic Ocean [*Mauritzen*, 1996; *Rudels et al.*, 2002] and in the Greenland, Iceland, and Norwegian Seas (the Nordic Seas) [*Swift et al.*, 1980], as well as from water undergoing deep wintertime convection in the Labrador [*Lazier*, 1973; *Talley and McCartney*, 1982; *Lilly et al.*, 1999; *Pickart et al.*, 1996; *Stramma et al.*, 2004] and Irminger [*Pickart et al.*, 2003] Seas. The component of NADW originating in the Nordic Seas enters the North

[1]Department of Applied Physics and Applied Mathematics, Columbia University, New York, New York, USA.
[2]Now at School of Mathematics and Statistics, University of New South Wales, Sydney, New South Wales, Australia.
[3]Also at NASA Goddard Institute for Space Studies, New York, New York, USA.
[4]Also at Department of Earth and Ocean Sciences, University of British Columbia, Vancouver, British Columbia, Canada.
[5]Department of Earth System Science, University of California, Irvine, California, USA.
[6]Lamont-Doherty Earth Observatory, Earth Institute at Columbia University, Palisades, New York, USA.

Copyright 2010 by the American Geophysical Union.
0148-0227/10/2009JC005750

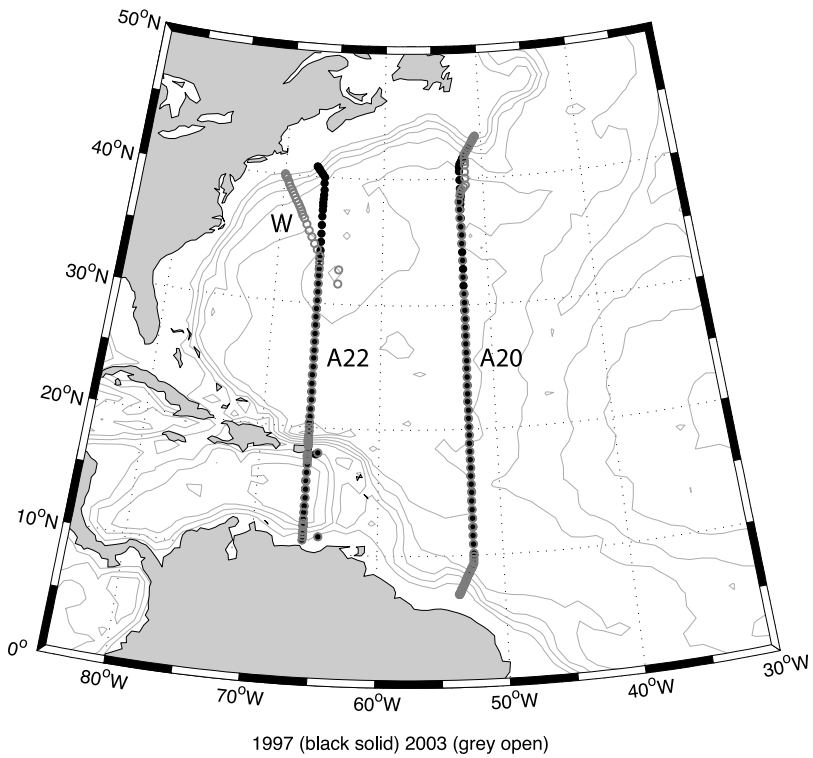

Figure 1. Stations along WOCE lines A20, A22, and W. The 1997 stations are indicated by solid black dots, and the 2003 stations are overlayed as grey circles. Bathymetry is contoured with a 1000 m interval.

Atlantic across the Greenland-Iceland-Scotland Ridge as overflow waters [*Ross*, 1984; *Dickson and Brown*, 1994; *Meincke*, 1983; *Saunders*, 1990; *Girton et al.*, 2001; *Hansen and Osterhus*, 2007], which entrain adjacent waters as they descend into the deep Atlantic [*Harvey and Theodorou*, 1986; *Dickson et al.*, 1990; *Tanhua et al.*, 2005]. NADW is transported equatorward by the Deep Western Boundary Current (DWBC) [e.g., *Swift*, 1984; *Dickson and Brown*, 1994; *Schmitz and McCartney*, 1993; *Rhein et al.*, 1995], forming the lower branch of the Atlantic Meridional Overturning Circulation.

[4] The compositions of the NADW components have been determined by classical temperature/salinity analysis [e.g., *Swift*, 1984; *Rudels et al.*, 2002] and the circulation pathways have been delineated by measuring the distribution of chlorofluorocarbons (CFCs) [e.g., *Weiss et al.*, 1985; *Smethie et al.*, 2000] and tritium [e.g., *Jenkins and Rhines*, 1980; *Doney and Jenkins*, 1994], which are incorporated in the NADW at its surface source regions [e.g., *Östlund and Rooth*, 1990; *Smethie*, 1993].

[5] The transit time for NADW to be transported from its source regions to the equator has been estimated from CFC [*Smethie et al.*, 2000; *Steinfeldt and Rhein*, 2004] and tritium/^{3}He ages [*Doney and Jenkins*, 1994] to be 25–30 years, which corresponds to a spreading rate of about 1–2 cm/s. This is considerably slower than the DWBC's measured speed of 5–25 cm/s [*Watts*, 1991; *Dickson and Brown*, 1994; *Bower and Hunt*, 2000]; the reason for this discrepancy is that most water parcels do not travel directly from the source region to the equator in the DWBC, but circulate into the basin interior where they are transported by the quasi-random action of eddies and mix with older water [e.g., *Hogg et al.*, 1986; *Schmitz and McCartney*, 1993; *Bower and Hunt*, 2000; *Steinfeldt et al.*, 2007]. The formation rate of NADW has been estimated from CFC inventories to be about 17–20 Sv [*Smethie and Fine*, 2001; *LeBel et al.*, 2008]. A more detailed review and description of NADW formation and circulation and the incorporation of CFCs into NADW can be found in the work by *Smethie et al.* [2000, 2007].

[6] Hydrographic sections A20 and A22 (as designated by the World Ocean Circulation Experiment (WOCE); Figure 1) traverse the North Atlantic's DWBC and CFC plume. Repeat hydrographies are available for both A20 and A22 from 1997 and 2003 cruises. We focus here only on line A20 because of its greater overlap between the 1997 and 2003 stations and because it lies almost entirely in the western North Atlantic basin, while A22 traverses the Caribbean for which key radiocarbon data was not available.

[7] This paper sets out to answer two central questions. The first question is where did the water in each of section A20's bottles last have surface contact and how long ago did that contact take place? Because each fluid element in the bottle will generally have taken a different path from the surface to the bottle, the question can be more precisely stated as "What is the joint distribution $\mathcal{G}(\mathbf{r}, t|\mathbf{r}_s, t-\tau)$ of last surface contact locations $\mathbf{r}_s$ and transit times τ from the surface that describes the admixture of waters in the bottle at location $\mathbf{r}$ and time t?" The distribution $\mathcal{G}$ (called a boundary propagator, a type of Green function) contains a huge amount of information. For every possible transit time interval and every possible surface patch, the distribution specifies the mass fraction of the bottle that came from that patch in that time interval. Because the only information we

have for each bottle is in the form of a few scalar quantities (T, S, and the concentrations of a few tracers), the problem of estimating $\mathcal{G}$ is highly underdetermined with far more unknowns than data constraints. Thus, the second question is "How well constrained is the ocean's $\mathcal{G}$ by the available sparse scalar data?"

[8] The boundary propagator $\mathcal{G}$ has been examined in some detail for ocean models [e.g., *Khatiwala et al.*, 2001; *Haine and Hall*, 2002; *Primeau*, 2005; *Peacock and Maltrud*, 2006]. However, the inference of $\mathcal{G}$ from tracer data has to date been much less explored. Studies of transit time distributions (TTDs) [e.g., *Waugh et al.*, 2004; *Tanhua et al.*, 2009] have used tracer data to fit the temporal dependence of $\mathcal{G}$ to parametric functions under the assumption of a single relevant end-member and at most two free parameters. Traditional water mass analyses utilizing the optimum multiparameter (OMP) method [e.g., *Tomczak*, 1981; *Tomczak and Large*, 1989], and its recent nonlocal refinements (parametric OMP [*de Brauwere et al.*, 2007]), use available tracer observations to infer the admixture of prespecified end-members regardless of the transit time from the surface. By predetermining the possible end-members and limiting their number to less than or equal the number of tracers, the OMP method avoids mathematical underdeterminedness. However, the OMP method is not able to determine all possible end-members (that is, all possible surface origins) from the data itself. Recently, *Kibler and Primeau* [2006] and *Primeau and Kibler* [2008] have used a maximum entropy (ME) method to invert the steady tracers of the WOAO5 database for the global distributions of the transit-time-integrated water mass fractions last ventilated in the ocean's major water mass formation regions. *Khatiwala et al.* [2009] applied a ME deconvolution to globally gridded data of both steady and transient tracers to estimate the transit-time-dependent boundary propagator Green functions at every grid point in the ocean for a surface tiling with 26 large regions. These Green functions were then convolved with the space- and time-varying history of anthropogenic carbon in the mixed layer estimated by placing physical and chemical constraints on the air-sea flux of CO_2.

[9] Here we use a maximum entropy method to invert hydrographic bottle data for both the transit time (temporal) and surface origin (spatial) dependence of the boundary propagator, $\mathcal{G}$. Integrating $\mathcal{G}(\mathbf{r}, t|\mathbf{r}_s, t-\tau)$ over surface locations $\mathbf{r}_s$ then yields TTDs, while integrating $\mathcal{G}$ over transit time τ gives the mass fraction of water at $(\mathbf{r}, t)$ that was last ventilated at surface location $\mathbf{r}_s$. The strength of the maximum entropy method [e.g., *Jaynes*, 1957; *Press et al.*, 2007] is that it regularizes the inversion problem in a way that introduces no biases other than those imposed by the data constraints: in the absence of the constraints, maximizing the information entropy distributes the fluid elements in the bottle uniformly, with respect to some prespecified weighting (see section 2.1), in terms of both surface origin and transit time. In addition, the information entropy itself provides a natural framework for estimating the uncertainty associated with the underdetermined nature of the inversions.

[10] The distribution $\mathcal{G}$ is closely related to the distribution of ventilation rates Φ of water that stays in the ocean interior for residence time τ or longer as introduced by *Primeau and Holzer* [2006] and *Hall et al.* [2007]. However, because Φ involves integrals of $\mathcal{G}$ over the entire ocean volume, we will leave estimates of Φ to a future study that will use deconvolutions for $\mathcal{G}$ at every point in the ocean. Here we focus only on line A20 to establish the character and degree of uncertainty of ME inversions for $\mathcal{G}$.

[11] The boundary propagator $\mathcal{G}$ encompasses information on where water was last ventilated and what the typical transit time from the mixed layer to a point in the interior is. As noted at the beginning, much of this information is known already. What is new here is that we use tracer data to directly constrain the entire joint distribution $\mathcal{G}$ of transit times and last surface contact locations, with rigorous uncertainty estimates for various key integrals of $\mathcal{G}$. Furthermore, we estimate $\mathcal{G}$ using an objective algorithm that does not require manual intervention.

2. Inversion Method

[12] The concentration $C_j^I(\mathbf{r}, t)$ of passive tracer species j at $(\mathbf{r}, t)$ can be represented as the admixture of values of the tracer at surface points $\mathbf{r}_s$ at earlier times t' via the convolution

$$C_j^I(\mathbf{r}, t) = \int d^2 r_s \int_{-\infty}^{t} dt'\, \mathcal{G}(\mathbf{r}, t|\mathbf{r}_s, t') C_j^S(\mathbf{r}_s, t') e^{-\gamma_j (t-t')}, \qquad (1)$$

where the boundary propagator Green function $\mathcal{G}$ is an integral representation of the transport from the surface [e.g., *Holzer and Hall*, 2000], and γ_j is the decay constant for radioactive species ($\gamma_j = 0$ for nonradioactive, chemically stable species). Although redundant, we use the superscripts I and S to clearly distinguish interior and surface tracer concentrations. Physically, $\mathcal{G} d^2 r_s dt'$ is the mass fraction of water at $(\mathbf{r}, t)$ that had its last surface contact with surface area $d^2 r_s$ during time interval $(t', t' + dt')$. For simplicity, and because the available tracer data is too sparse in both time and space to allow a more detailed analysis, we now assume that oceanic transport is cyclostationary, that is, that the ocean's transport operator repeats itself every year with the same seasonal cycle. The propagator $\mathcal{G}$ is therefore only a function of the number of years, n, elapsed from the year containing t, and the time of year of both t and t'. Because seasonally varying hydrographic data is typically available as monthly means, we now immediately discretize the time of year to 12 months (taken equally long for convenience), with m being the month of t' and m_0 being the month of t. We also discretize the surface of the ocean into patches ($5° \times 5°$ boxes here) of area A_s, where s is the index of the surface patches. Thus, using the probability notation $\mathcal{P}(s, n, m|\mathbf{r}, m_0)$ for the discretized version of $\mathcal{G} d^2 r_s dt'$, we have for each tracer species j

$$\begin{aligned} C_j^I(\mathbf{r}, t) &= \sum_s \sum_{n=0}^{\infty} \sum_{m=1}^{M(n)} \mathcal{P}(s, m, n|\mathbf{r}, m_0) C_j^S(s, t - \tau_{n,m}) e^{-\gamma_j \tau_{n,m}} \\ &\equiv \hat{C}_j^I[\mathcal{P}], \end{aligned} \qquad (2)$$

where

$$\tau_{n,m} = [n + (m_0 - m)/12]\tau_a, \qquad (3)$$

with $\tau_a = 1$ a and $M(0) = m_0$ and $M(n) = 12$ for $n > 0$. Equation (2) also defines the notation $\hat{C}_j^I[\mathcal{P}]$ for the value of the interior tracer concentration obtained by propagating the

boundary conditions C_j^S with a given $\mathcal{P}$. Physically, $\mathcal{P}(s, n, m|\mathbf{r}, m_0)$ is the mass fraction of water at $\mathbf{r}$ during month m_0 that had last contact with the sth surface patch n years ago during month m, that is, a time $\tau_{n,m}$ ago. Equivalently, $\mathcal{P}(s, n, m|\mathbf{r}, m_0)$ is the probability that a fluid element had last surface contact with patch s a time $\tau_{m,n}$ ago, conditional on the fluid element currently being at $\mathbf{r}$ during month of year m_0. Because all the water at $(\mathbf{r}, m_0)$ must have had surface contact somewhere at some time in the past, $\mathcal{P}$ has the normalization

$$\sum_{s,n,m} \mathcal{P}(s, m, n|\mathbf{r}, m_0) = 1. \tag{4}$$

2.1. Information Entropy, $\mathcal{S}$

[13] To quantify the information provided by the tracer data for constraining the boundary propagator, we capitalize on the boundary propagator's probabilistic interpretation to construct the Shannon information entropy [*Shannon*, 1951]

$$\mathcal{S} = -\sum_{s,n,m} \mathcal{P} \log \frac{\mathcal{P}}{\mu}, \tag{5}$$

where $\mu(s, n, m|\mathbf{r}, m_0)$ is a measure or "prior" whose significance will be clear shortly.

[14] We now invoke the principle of maximum entropy [*Jaynes*, 1957], which asserts that the best choice for $\mathcal{P}$ is that which is maximally noncommittal with regard to missing information by maximizing $\mathcal{S}$ subject to any data constraints. In the absence of data error, the $\mathcal{P}$ that maximizes $\mathcal{S}$ is therefore identified with the most probable function $\mathcal{P}$ [e.g., *Skilling and Gull*, 1991; *Press et al.*, 2007].

[15] Maximizing $\mathcal{S}$ without any data constraints yields $\mathcal{P} = \mu$, that is, in the absence of tracer information the probability of water having had surface contact some transit time ago is spread as widely as possible over the surface and over transit time with measure μ. The strength of the ME method lies precisely in this broad, noncommittal spread of probability. No surface patches or transit times are a priori excluded unless they are explicitly forbidden by having zero μ. In the sense that $\mathcal{P}$ reduces to μ in the absence of any data, we consider μ to be a prior guess at $\mathcal{P}$, or simply a prior, for short. Note that $\mathcal{S} \leq 0$, with a global maximum of $\mathcal{S} = 0$ at $\mathcal{P} = \mu$.

[16] In order to quantify the uncertainty associated with the underdetermined nature of finding $\mathcal{P}$, we need to know how likely functions $\mathcal{P}$ are that do not maximize the constrained entropy, but that still satisfy the data constraints. By assuming that all possible $\mathcal{P}$ (for our problem, all possible admixtures of surface origin and transit time) that are consistent with the data constraints are equally likely relative to measure μ, the probability distribution of $\mathcal{P}$ conditional on the data can be argued to be $\mathrm{Prob}(\mathcal{P}|C) \propto \exp(\alpha\mathcal{S} - \chi^2/2)$ [e.g., *Skilling and Gull*, 1991; *Press et al.*, 2007] for Gaussian data errors. Here χ^2 is the usual nondimensional measure of the misfit $C_j^I - \hat{C}_j^I[\mathcal{P}]$ relative to the data uncertainty and the yet undetermined parameter α controls the relative importance of entropy and χ^2.

[17] The most probable $\mathcal{P}$ thus maximizes $\mathcal{H} \equiv \alpha\mathcal{S} - \chi^2/2$. However, if the data has finite uncertainty so that $\exp(-\chi^2/2)$ is not sharply peaked, finding the maximum of $\mathcal{H}$ is a very large scale optimization problem. We avoid large-scale optimization here by first maximizing $\mathcal{H}$ while enforcing zero misfit ($\chi^2 = 0$). Maximizing $\mathcal{H}$ then reduces to the maximum entropy principle and the optimization reduces to the problem of finding a few Lagrange multipliers, as described below. The full distribution $\mathrm{Prob}(\mathcal{P}|C)$, which allows for finite data errors, can then formally be constructed by integrating $\exp(\alpha S)$ subject to hard data constraints over a multivariate Gaussian ensemble of such data constraints. In this paper, we therefore first determine the maximum of the entropy for zero data misfit and quantify the corresponding purely entropic part of the distribution of $\mathcal{P}$, proportional to $\exp(\alpha S)$. We then calculate the effect of finite data errors by performing an approximate Monte Carlo integration over a Gaussian ensemble of data constraints as described in section 5.

[18] Following the arguments of *Skilling and Gull* [1991], we choose $\alpha = -\frac{N}{2\mathcal{S}_{\max}}$, where $\mathcal{S}_{\max}$ is the maximum of the data-constrained entropy, and N is the number of effective constraints on $\mathcal{P}$ provided by the data. (For perfectly nonredundant data, this choice of α reduces to $\chi^2 = N$, where N is the number of data constraints [*Skilling and Gull*, 1991; *Press et al.*, 2007].) If $\mathcal{P}^*$ denotes the $\mathcal{P}$ that maximizes the constrained entropy, we then have that the probability of any other possible function $\mathcal{P}$, conditional on definite, zero-misfit data constraints, is given by

$$\mathrm{Prob}(\mathcal{P}) \propto \exp\left(-\frac{N}{2}\frac{\mathcal{S}[\mathcal{P}]}{\mathcal{S}[\mathcal{P}^*]}\right). \tag{6}$$

In analogy with statistical mechanics [e.g., *Press et al.*, 2007], we may think of the right-hand side of (6) as a "multiplicity" that quantifies the number of possible functions $\mathcal{P}$ (that is, the number of possible admixtures) that are consistent with the data constraints. Equation (6) makes clear that we are interested here not in how the absolute information entropy is reduced as $\mathcal{P}$ deviates from $\mathcal{P}^*$, but only in how much it is reduced relative to the maximum allowed by the data.

[19] The $\mathcal{P}$ that maximizes the entropy is forced to satisfy the data constraints by introducing the Lagrange multipliers λ_j:

$$\mathcal{S} = -\sum_{s,n,m} \mathcal{P} \log \frac{\mathcal{P}}{\mu} + \sum_{j=1}^{J} \lambda_j (C_j^I - \hat{C}_j^I[\mathcal{P}]), \tag{7}$$

where $\hat{C}_j^I[\mathcal{P}]$ is defined by the RHS of equation (2). The solution $\mathcal{P}$ which maximizes the constrained entropy (7), and thereby deconvolves equation (2) by finding $\mathcal{P}$ given the tracer concentrations, is obtained by setting the functional derivative of (7) with respect to $\mathcal{P}$ to zero. One obtains

$$\mathcal{P} = \frac{\mu}{Z} \exp\left(-\sum_j \lambda_j C_j^S(s, t - \tau_{n,m})\, e^{-\gamma_j \tau_{n,m}}\right), \tag{8}$$

where $\mathcal{P}$ is normalized by the "partition function" Z given by

$$Z = \sum_{s,n,m} \mu(s, n, m|\mathbf{r}, m_0) \exp\left(-\sum_j \lambda_j C_j^S(s, t - \tau_{n,m}) e^{-\gamma_j \tau_{n,m}}\right). \tag{9}$$

The J Lagrange multipliers are found by substituting (8) into the J constraint equations (2) and solving for the λ_j. We have thus regularized a grossly underdetermined problem by reducing it to a system of J equations in J unknowns. Note that the equations are nonlinear in the λ_j. We also emphasize that a solution to the constraint equations (2) means that $C_j^I - \hat{C}_j^I[\mathcal{P}] = 0$, that is, the ME solution for the boundary propagator $\mathcal{P}$ satisfies its tracer constraints exactly.

2.2. Choice of Prior Measure, μ

[20] We consider a uniform prior and a prior based on coarse-resolution solutions of a steady advection-diffusion equation. The uniform prior has the property that in the absence of any information all surface locations and all times since last contact, up to some maximum time $\tau_{\max}$, are equally likely. Hence the probability of having last contact with patch s is just proportional to its area A_s, with all $\tau_{n,m}$ up to $\tau_{\max}$ being equally likely. The uniform prior is thus given by

$$\mu(s, n, m|\mathbf{r}, m_0) = \frac{A_s}{A}\frac{\Delta\tau}{\tau_{\max}} \tag{10}$$

for $\tau_{n,m} < \tau_{\max}$, and $\mu = 0$, otherwise, with $\Delta\tau = 1$ month. We choose $\tau_{\max} = 4000$ a, and found our results to be insensitive to the precise value of $\tau_{\max}$.

[21] The uniform prior assumes essentially zero knowledge about the ocean circulation, which begs the question how different are the deconvolutions if we use a prior that does build in knowledge of the circulation and would this lead to results that are more certain? To answer this question, we built a second prior by solving a steady advection-diffusion equation for the ocean using a coarse-resolution integration as described by *Primeau* [2005]. We refer to this as the advective-diffusive (AD) prior. The required advection-diffusion operator was constructed from the time-averaged velocity and eddy diffusivity tensor fields computed by a dynamical OGCM. The OGCM is based on the NCAR CSM Ocean Model [*Pacanowski et al.*, 1993] and has 29 vertical levels with thicknesses ranging from 50 m near the surface to 300 m for the deepest level and a horizontal resolution of ~3.75° × 3.75°. The spatial discretization is based on second-order centered differences. The eddy diffusivity tensor is computed using the k profile vertical mixing scheme (KPP [*Large et al.*, 1994]) and the GM isopycnal eddy-mixing scheme [*Gent and McWilliams*, 1990]. The background diapycnal and isopycnal diffusivities are 0.5×10^{-5} and 1000 m^2/s. The OGCM was forced with seasonally varying surface momentum and buoyancy fluxes. The strength of the model's meridional overturning stream function is ~18 Sv. The water mass ventilation properties of the annually averaged circulation has been described in detail in previous publications. In particular, transit time distributions at various positions in the Atlantic are shown in Figure 11 of *Primeau* [2005] and his Figure 4 displays the fractions of water across a section at 30°W that were ventilated through various surface regions. The annually averaged advection-diffusion operator's ventilation rate distribution is described by *Primeau and Holzer* [2006] and its surface-to-surface transport pathways are discussed by *Holzer and Primeau* [2006, 2008].

[22] The patch-integrated boundary propagator Green functions $\mathcal{G}(\mathbf{r}, \tau|\Omega_i)$, where the patches Ω_i tile the ocean surface as shown in Figure C1, were computed as the response to a delta function surface concentration boundary condition on Ω_i with zero concentration enforced elsewhere on the surface [*Holzer and Hall*, 2000; *Primeau*, 2005]. To construct the AD prior, the coarse-grained Green function was redistributed over 5° × 5° grid boxes such that

$$\mu_{AD}(s, n, m|\mathbf{r}, m_0) = \frac{A_s}{A(\Omega_i)}\,\mathcal{G}(\mathbf{r}, \tau_{n,m}|\Omega_i), \tag{11}$$

where A_s is the area of the 5° × 5° grid box labeled by s and $A(\Omega_i)$ is the area of patch Ω_i that contains surface box s. The purpose of coarse graining $\mathcal{G}$ in this way is to ensure that the AD prior is not overly influenced by small-scale features in the model's circulation that cannot be expected to be accurate. It is therefore worth pointing out that while the information in the publications cited above that describe the model's surface-to-surface transport is relevant to understanding the model's circulation, most of this information is not directly encoded in the AD prior because of the relatively large size of the patches used to compute $\mathcal{G}$. The relevant information captured by the AD prior is summarized in Figure C2. Figure C2a shows the profiles of the distributions of times since last surface contact obtained from the AD prior (without enforcing any tracer constraints) and Figure C2b shows the AD prior's ideal mean age.

[23] Because we found that the inversions with a uniform prior tended to give unrealistically large fractions of Mediterranean water, and because our advective-diffusive solution did not include the Mediterranean at all, we replaced the Mediterranean's surface boundary condition with a boundary condition along a vertical wall across the Strait of Gibraltar. In the 1° × 1° data sets the Strait of Gibraltar is a single vertical profile. In the case of the uniform prior the contribution of a vertical wall layer of width Δz was represented by $(\Delta z/D)(A_M/A)(\Delta\tau/\tau_{\max})$, where D is the depth of the strait and A_M and A are the areas of the Mediterranean and the global ocean. In the case of the AD prior, the time dependence of the Mediterranean part of the prior was taken to be a normalized inverse Gaussian, $\mathcal{I} \equiv \exp[-(\tau - \Gamma)^2/(4\Delta^2\tau/\Gamma)]/\sqrt{4\Delta\delta^2(\tau/\Gamma)^3}$, with $\Gamma = \Delta$ and a mean age parameter $\Gamma(\mathbf{r})$ that depends on the depth of the bottle according to the section-averaged global ideal mean age of the advective-diffusive solution, scaled to 30 a at the surface (which corresponds to a mode of $\mathcal{I}$ at 4.9 a). The choice of an inverse Gaussian form is motivated by the fact that model transit time distributions for single end-members can be well fit by this form, and parametric inversions of tracer data using inverse Gaussians [e.g., *Waugh et al.*, 2004] suggest $\Gamma = \Delta$ is appropriate for the ocean.

3. Data

[24] Because our method relies on scalar quantities that are either conserved in the ocean interior or decay with known time constants, we computed potential temperature θ and the quasi-conserved tracer $PO_4^* \equiv PO_4 + O_2/175$ [*Broecker et al.*, 1998]. Our inversions are thus based on the following set of tracers: θ, S, PO_4^*, CFC-11, and ^{14}C.

Because CFC-11 is transient on a decadal timescale, the CFC-11 values from the 1997 and 2003 cruises were used separately. We acknowledge that PO_4^* is not a precisely conserved tracer and that there is uncertainty in the 1:175 stoichiometry [*Anderson and Sarmiento*, 1994]. The Monte Carlo uncertainty analysis described below could in principle be used to investigate the effect of these uncertainties, although their effect is likely to be dominated by the uncertainties that come from the underdeterminedness of the problem ("entropic" uncertainties; see below). The A20 hydrographic data also includes CFC-12, but because the shape of the CFC-12 atmospheric time history prior to ~1992 is very similar to that of CFC-11, and because we are interested here in timescales of decades to centuries, we did not use CFC-12 for added computational efficiency. Because our focus is on deep waters, we do not consider the upper 250 m to reduce the computational burden, and also because interannual variability makes the assumption of cyclostationarity particularly poor for the upper ocean. The A20 data also includes carbon tetrachloride (CCl_4) measurements, but this tracer is not stable and recent estimates of its loss rate are themselves based on parametric inversions for TTDs [e.g., *Waugh et al.*, 2004; *Huhn et al.*, 2008]. We do not consider CCl_4 here because correcting for its loss would considerably complicate our analyses. We also note that while CCl_4 contains transport information for timescales up to ~100 a, CCl_4 does not fill the large gap in timescales between CFCs and radiocarbon.

3.1. Surface Boundary Conditions

[25] The surface boundary conditions for T, S, O_2, and PO_4 are taken from the World Ocean Atlas 2005 (WOA05) [*Locarnini et al.*, 2006; *Antonov et al.*, 2006; *Garcia et al.*, 2006a, 2006b], while the boundary condition for natural ("prebomb") $\Delta^{14}C$ and the CFCs were taken from the Global Ocean Data Analysis Project (GLODAP) data set [*Key et al.*, 2004; *Sabine et al.*, 2005]. For θ, S, and PO_4^* monthly data were used, while the GLODAP data set provides annual averages for $\Delta^{14}C$. The time-evolving CFC boundary conditions were constructed from the surface values of the GLODAP data set, which represents annual mean mixed layer CFC concentrations for the nominal year of 1994. Mixed layer concentrations for other years were then simply obtained by scaling the boundary condition for 1994 to the time series of the atmosphere by multiplying the 1994 GLODAP surface field by $CFC(n)_A/CFC(1994)_A$, where $CFC(n)_A$ is the measured, globally averaged atmospheric concentration for year n, taken from the work of *Walker et al.* [2000]. This implicitly accounts for the CFC subsaturation, although the implied saturation level is time-independent.

[26] The GLODAP domain is unfortunately smaller than the WOA05 domain, and does not include many marginal seas such as the Caribbean Sea and the ocean north of 62.5°N. We therefore extended the CFC and $\Delta^{14}C$ boundary conditions zonally from their edges to the boundaries of the 1° × 1° WOA05 domain. For $\Delta^{14}C$, the missing northern regions were simply pegged at a value of −53 per mil. For the CFCs we computed the missing northern values from the atmospheric concentration using the coefficients of *Warner and Weiss* [1985] and by specifying a saturation that smoothly interpolates from the northern edge of the GLODAP data into the Arctic, where measurements suggest saturations near 100% [*Tanhua et al.*, 2009]. The saturation was taken to have the latitudinal profile $70\% + 30\%[1 - \exp(-0.006(\phi - 62.5)^2)]$, where ϕ is latitude in degrees. Given that this profile is somewhat arbitrary, known temporal changes in saturation in the Arctic from 85% to 100% over the last two decades were ignored.

3.2. Interior Data

[27] For the interior concentrations of tracers other than radiocarbon we used the A20 bottle data available from the CLIVAR and Carbon Hydrographic Data Office (http://cchdo.ucsd.edu). These data were measured during 1997 (late July to early August) and 2003 (late September to early October). Where the horizontal positions of the 1997 and 2003 profiles were closer than 0.16° latitude and 0.6° longitude, the 2003 data was deemed to have the 1997 horizontal position and was vertically interpolated to 1997 bottle depths. Figure 2 summarizes the 1997 bottle locations and for which locations repeat hydrography was available. For the transient CFC-11, the 1997 and 2003 values were used separately. For the other tracers, the 1997 and 2003 values were averaged (and also used to estimate variability; see Appendix B). The interior concentrations of radiocarbon at the 1997 bottle locations were obtained by interpolating from the gridded GLODAP data set.

[28] Contour plots of the A20 hydrographic data from the 1997 cruise, including θ, S, neutral density, and nutrients can be found in the paper by *Hall et al.* [2004]. In Figure 3 we only show the key transient tracers: CFC-11 for 1997 and 2003 from the cruise data and $\Delta^{14}C$ from GLODAP. The prominent features of the CFCs are high concentrations in the upper ocean, a pronounced CFC plume in the northern part of the section at middepth between ~0.5 and ~2.5 km, and more dilute concentrations where the DWBC recrosses the southern part of the section. As expected, CFC concentrations increase from 1997 to 2003. The $\Delta^{14}C$ data shows greatest depletion in the abyssal waters and a tongue of relatively depleted water in the southern part of the section between ~500 and ~1500 m depth. This tongue likely represents Antarctic Intermediate Water (AAIW); see also below.

[29] Our boundary conditions and the interior tracer data have uncertainties that are important for our analysis. They are further discussed in the section on uncertainty analysis below, with additional details provided in Appendix B.

4. Results

4.1. Water Mass Fractions

[30] The local mass fraction of water that was last ventilated on surface patch s year τ ago or longer (also referred to as the water mass fraction from s of age τ or older) is given by

$$f(s,\tau|\mathbf{r},m_0) \equiv \sum_{n\geq\tau}\sum_{m}\mathcal{P}(s,m,n|\mathbf{r},m_0). \tag{12}$$

Figure 4 shows the water mass fraction regardless of transit time ($f(s, 0|\mathbf{r}, m_0)$, all transit times (n, m) are summed) for three particular bottle locations. One bottle was chosen in the middepth CFC plume in the northern part of the section

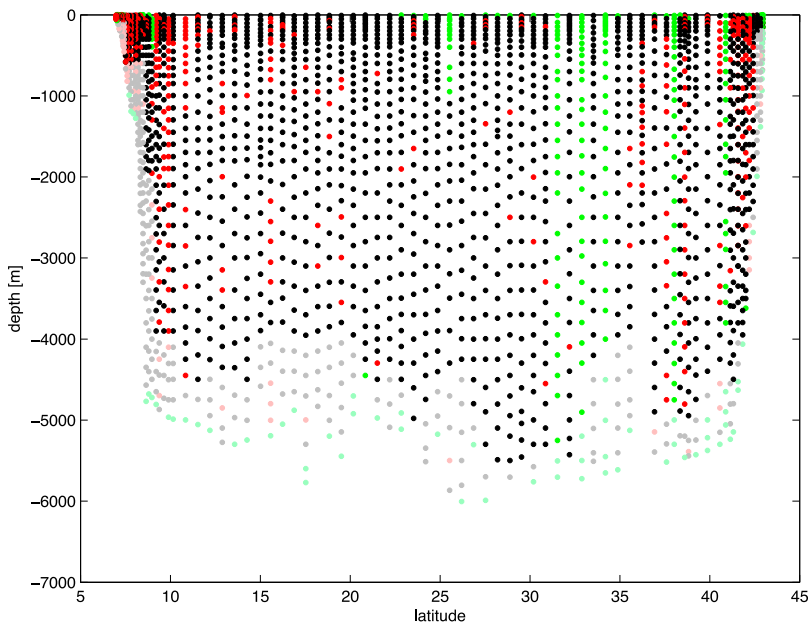

Figure 2. The locations of the bottle data used along WOCE line A20. The color of the location indicates whether data was available from only one or from both cruises. Black, both 1997 and 2003. Green, only 1997. Red, only 2003. The lighter colored locations lie outside the GLODAP grid for ^{14}C and were not used in this study.

(36.9°N, 1650 m), another in the extension of the plume further south (20.8°N, 1350 m), and a third in the abyssal basin (29.5°N, 4604 m). The patterns shown are typical and not sensitive to the exact location of the bottles. Figure 4 shows the fs for the cases of the uniform and the AD prior, each with and without CFC-11. Only the northern North Atlantic and the Nordic and Barents Seas are shown, where the patterns are concentrated (the precise fractions integrated over larger regions are quantified below). While the oceans elsewhere also contribute to these bottles, such contributions are smaller and/or not as localized.

[31] The pattern for the bottle in the northern middepth CFC plume (Figure 4, top) identifies the Labrador, Irminger, and Nordic Seas as significant source regions ("end-members"). The uniform prior yields overall lower fractions (note the factor of 2 used for plotting) than the AD prior and also shows some contribution from the Barents Sea. The AD prior with CFC-11 places the greatest emphasis on the Labrador Sea, approximately where Labrador Sea Water is thought to form [see, e.g., *LeBel et al.*, 2008]. Interestingly, the differences between the cases with and without CFCs are modest, which means that much of the available information on the water mass fraction regardless of residence time is encoded in θ, S, PO_4^*, and possibly ^{14}C. The bottle further south (Figure 4, middle) shows similar spatial patterns, but of reduced amplitude. This is consistent with the expectation that those waters are older (having been in contact with the atmosphere when its CFC-11 was lower) and that waters from other regions become mixed in as NADW spreads southward. The bottle in the abyssal North Atlantic (Figure 4, bottom) does not have the Labrador Sea component but contains significant fractions of Greenland Sea Water, with the uniform prior case also having prominent contributions from the Barents Sea.

[32] We now focus on the water mass fraction of age τ or older as a function of depth, latitude, and τ. Based on the patterns of Figure 4, we define the regional surface masks of Figure 5. Region L encompasses the Labrador and Irminger Seas, while region N encompasses the Greenland, Norwegian, and Barents Seas. In addition, we also define a Southern Ocean region SO as the ocean south of 50°S and region G, the global world ocean (which includes L, N, and SO). With these region masks R, we compute the regionally integrated water mass fractions of age τ or older $f_R(\tau|\mathbf{r}, m_0) = \sum_{s\in R} f(s, \tau|\mathbf{r}, m_0)$. The water mass fractions for regions R = L, N, L + N, SO, and G, are shown in Figure 6 for waters of any age, older than 39 a, and older than 160 a for the case of the AD prior with CFC-11. (The differences between this and the case of the uniform prior are examined below.) The threshold values of 39 a and 160 a were chosen based on the detailed dependence of $f_R(\tau|\mathbf{r}, m_0)$ on τ for the regions L + N and SO, respectively, which will be discussed in detail below (Figure 7). The precise numerical values of the thresholds are not significant and merely reflect the available transit times in our coarse-grained set of τ (Appendix A).

[33] Consider first the water mass fraction regardless of transit time (Figure 6, top). The L fraction is stretched out in a band between ~1 and ~2 km depth, the expected depth range for Labrador Sea Water [e.g., *LeBel et al.*, 2008], with local maxima reaching 35% (note the factor of 2 applied for plotting). If we use f_L to compute a weighted average of $\sigma_{1.5}$ across the section, we obtain $\sigma_{1.5}$ = 34.6, consistent with the density of Classical and Upper Labrador Sea Water [e.g., *Pickart and Smethie*, 1998]. The waters identified by f_N lie primarily below the L waters, although there is significant overlap. The highest N fractions of ~80% are found below ~3000 m in the northern half of the section. These waters are consistent with overflow waters, that were last ventilated

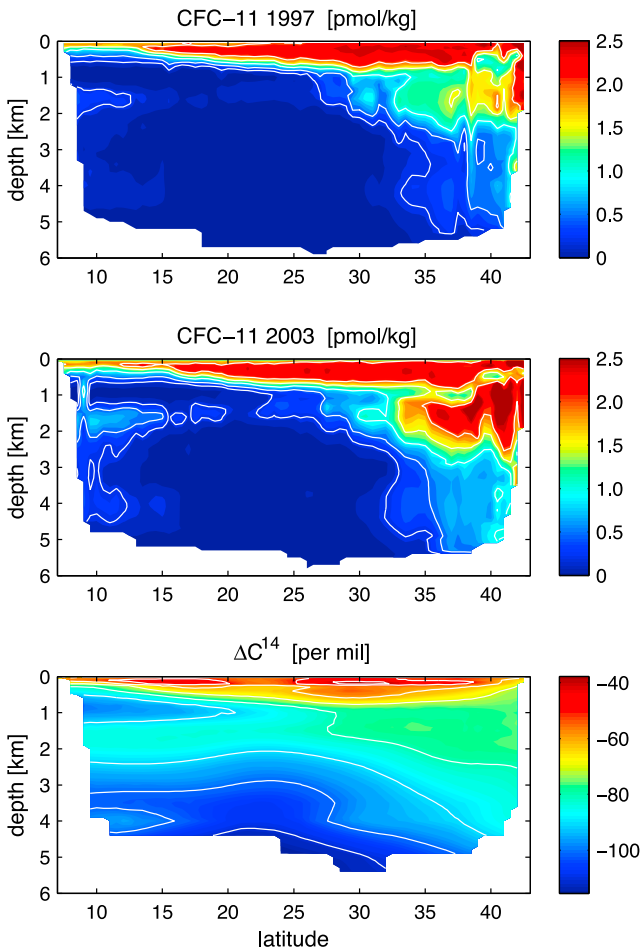

Figure 3. The transient tracers at the longitude of line A20 (~52°W) used in this study: the CFC-11 bottle data from the 1997 and 2003 line A20 cruises and the natural Δ^{14}C data of the GLODAP data set. For CFC-11 white contour lines are plotted at 0.25, 0.5, 1, 1.5, and 2 pmol/kg, while for the Δ^{14}C white contour lines are plotted every 10 per mil.

in the Nordic and/or Barents Seas (see also Figure 4). A f_N-weighted density average yields $\sigma_{1.5}$ = 34.7 and σ_4 = 45.7 (45.8 if only waters older than 160 a are considered), which is also broadly consistent with overflow waters [e.g., *Pickart and Smethie*, 1998]. The sum of the L and N fraction shows that these waters dominate the North Atlantic below the thermocline between 1 and 3 km depth, with fractions in excess of ~75%.

[34] Southern Ocean waters identified by f_{SO} are seen to constitute up to ~30% of abyssal waters. Note that where the f_{SO} fraction is large at depth, the f_{L+N} fraction is correspondingly lower, which shows that abyssal waters are dominated primarily by Labrador Sea, overflow, and Southern Ocean waters, as expected. There is also a tongue of SO waters in the southern portion of the section between ~500 and ~1000 m with fractions up to ~50%. This tongue of SO water represents AAIW possibly formed as Subantarctic mode water, which has been implicated as an important source of nutrients to the North Atlantic [*Sarmiento et al.*, 2004; *Williams et al.*, 2006]. The pattern of this AAIW tongue appears to be due to the colocated tongue of depleted (older) Δ^{14}C visible in Figure 3. The global water mass fraction f_G regardless of age must be unity, as expressed by equation (4).

[35] It is very interesting to further partition the water mass fractions according to when they had last contact with the surface. To this end, Figure 6 (middle) and Figure 6 (bottom) show the water mass fractions older than 39 and 160 a, respectively. This shows that the portion of the L fraction in the vicinity of the northern middepth CFC plume was last ventilated less than 39 a ago, while much of the southern portion is older than 39 a. Virtually none of the L fraction is older than 160 a, which means that L waters older than that have either been transported elsewhere or that L waters return to the mixed layer with a surface-to-surface transit time of less than 160 a.

[36] The N fraction of overflow waters in the northern part of the section between ~1 and ~3 km depth displays similar behavior to the L fraction, with the bulk of the N fraction there having been last ventilated less than 39 a ago. However, unlike the L fraction, overflow waters older than 160 a can be found below ~3500 m, with mass fractions of around 50%. Thus, approximately half of the deep water in the western North Atlantic is overflow water ventilated in the Nordic and/or Barents Seas more than ~160 a ago. The patterns of the L + N fraction simply summarize the behavior of both water types.

[37] The SO water mass fraction is everywhere older than 39 a, as expected of waters of such remote origin, while the abyssal SO fraction is older than 160 a. The tongue of SO water that identifies AAIW is younger then 160 a, and a more detailed analysis shows most of it to be younger than ~100 a.

[38] The mass fraction regardless of where at the surface last contact occurred, f_G, shows that the thermocline (the blue patch sloping up toward the equator) and the vicinity of the northern middepth CFC plume are filled with waters that were ventilated less than 39 a ago. Waters older than 160 a are found primarily below ~3000 m.

[39] To show the detailed dependence of $f_R(\tau|\mathbf{r}, m_0)$ on τ, and to contrast the four inversion cases, we now consider $f_R(\tau|\mathbf{r}, m_0)$ vertically averaged over slabs as a function of latitude and τ. Figure 7 shows such space-time plots for the slabs containing the bulk of the L and N waters and the tongue of AAIW. Figure 7 shows that when using a uniform prior, the CFC-11 data is crucial for capturing the fact that the L (Labrador/Irminger Sea) and N (overflow) waters in the northern part of the section above ~3 km are relatively young. Leaving out CFC-11 with the AD prior still gives reasonable results because the AD prior already encodes the information that the northern portion of the section at middepths is relatively young.

[40] With the exception of the no-CFC uniform case, the patterns of Figure 7 show the L and N water mass fractions being several decades younger in the northern part of the section than in the southern part. This is consistent with the fact that these waters propagate around the Atlantic basin in the direction of the DWBC. However, the advective timescale for the DWBC with velocities of ~5 cm/s [e.g., *Pickart and Smethie*, 1998] over ~3000 km is only ~2 a. The fact that the transit time difference between the northern and southern parts of the section is decades rather than years

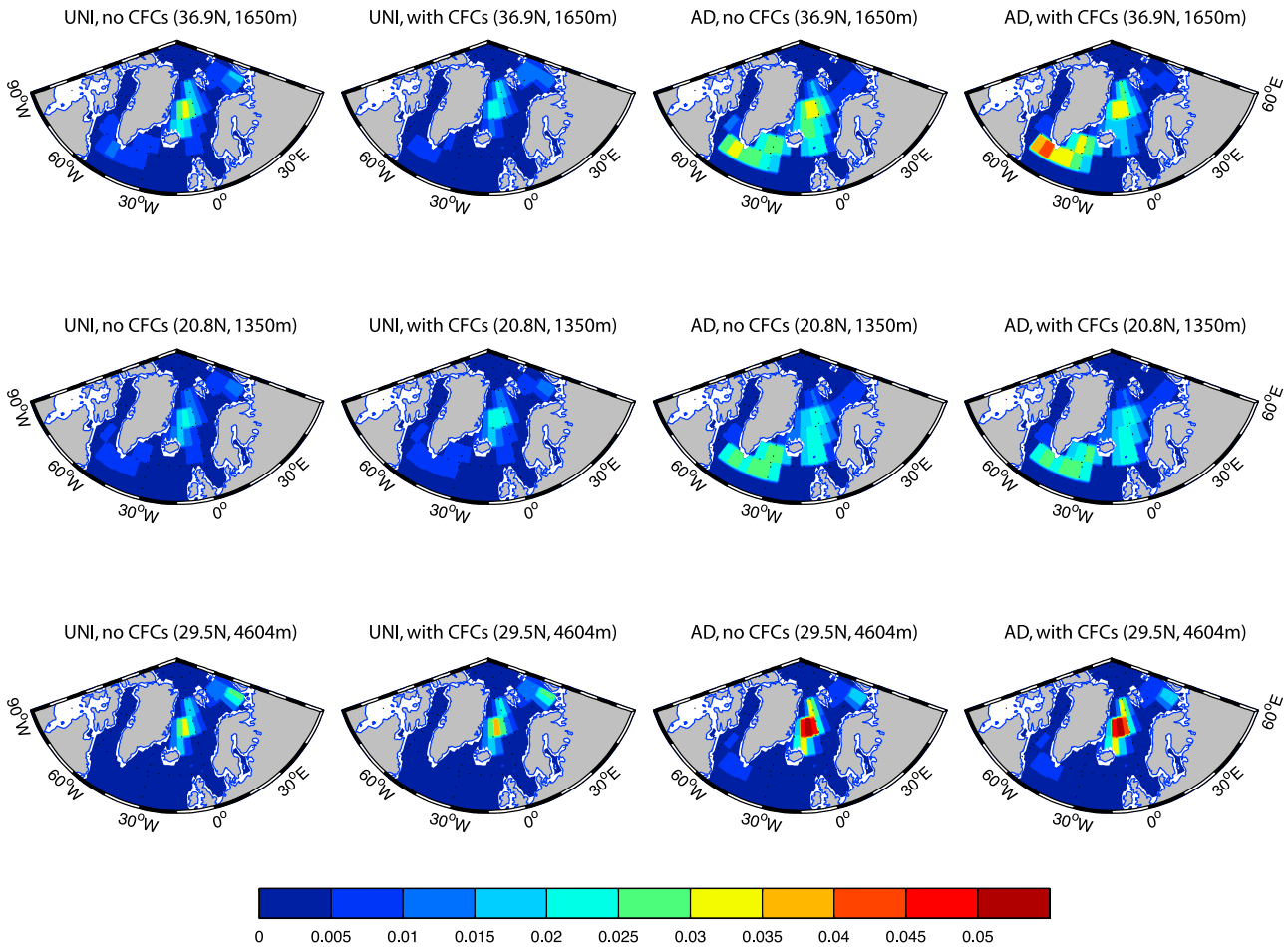

Figure 4. The water mass fraction from each 5° × 5° surface patch regardless of transit time for the three bottle locations indicated. Note that these are the dimensionless fractions, not the fractions per unit area.

shows that much of the transport is not due to direct advection by the DWBC, but instead must involve recirculations and quasi-random mixing by mesoscale eddies. This is also supported by the fact that the L and N fractions are distributed over a much broader range of transit times in the southern part of the section than in the northern part (Figure 7). We note that these results are consistent with the "diffusive conveyor" picture of *Holzer and Primeau* [2006, 2008].

[41] As expected, CFCs play a minor role for the inversions of the SO water mass fraction. The temporal information of the SO waters is driven by ^{14}C, the only transient tracer used with time dependence beyond ~75 a. As a consequence, all four cases of the inversions show a similar SO pattern with the AAIW tongue having been ventilated primarily less than ~100 a ago.

[42] The 3500 m-to-bottom averaged f_N and f_{SO} (not shown) are the oldest fractions considered here. These vertically averaged fractions of age τ or older drop to about a tenth of the corresponding fractions of age zero or older for $\tau \sim 600$ to 700 a, with the SO fractions having the longer transit times. Thus, the majority of the abyssal N and SO waters in the North Atlantic are either ventilated or transported to different parts of the ocean after roughly half a millennium.

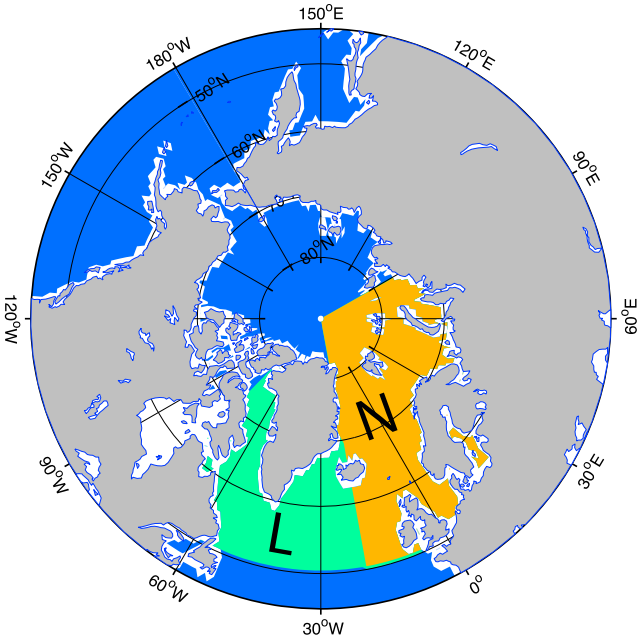

Figure 5. The surface masks used to define water mass fractions: L (green) includes the Labrador and Irminger Seas, while N (orange) includes the Nordic and Barents Seas.

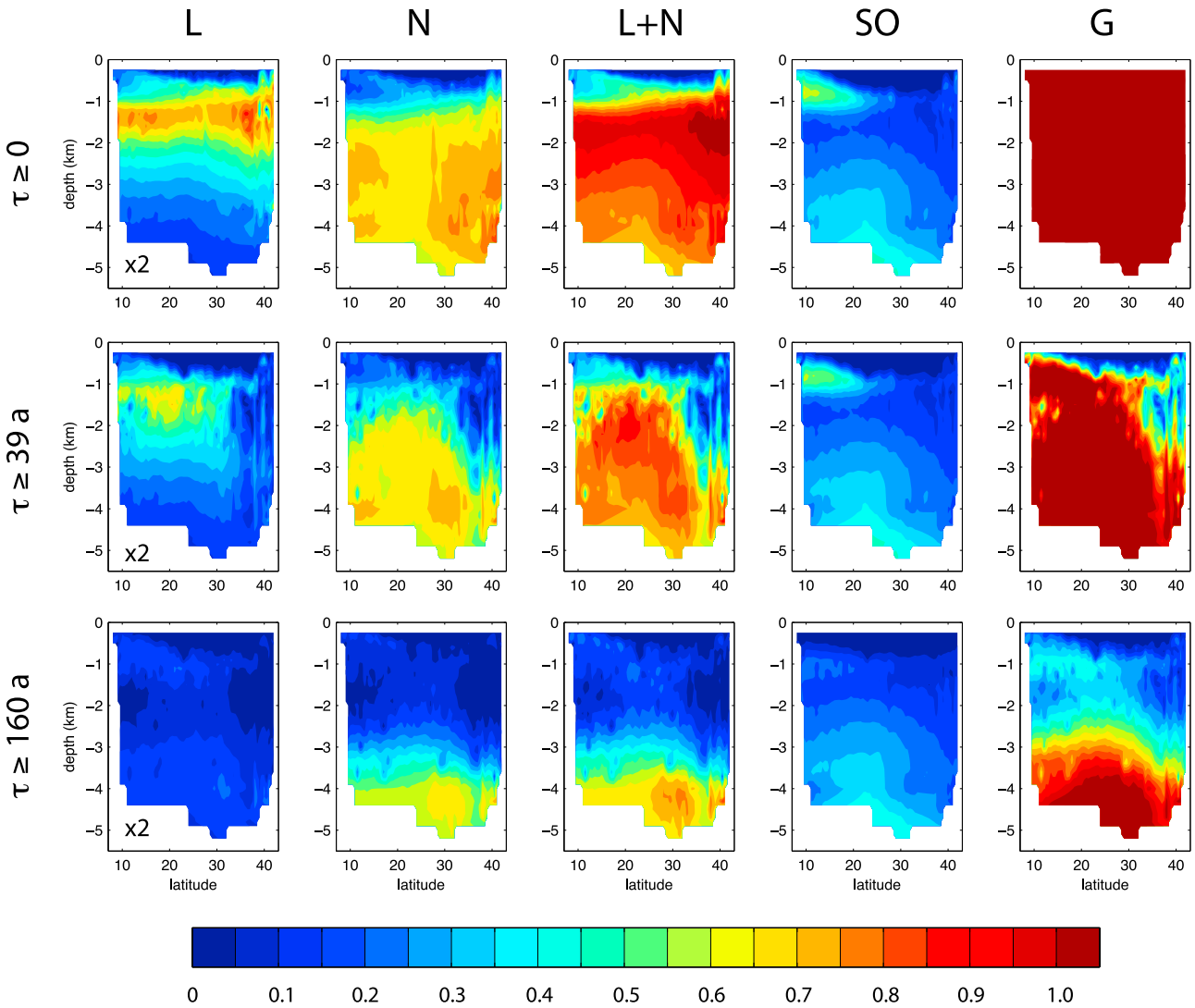

Figure 6. The water mass fractions of age τ or older from our L and N patches, the union of these (L + N), the Southern Ocean south of 50°S (SO), and the entire global ocean surface (G), as computed using the AD prior with CFC-11. The age thresholds are (top) $\tau \geq 0$, (middle) $\tau \geq 39$ a, and (bottom) $\tau \geq 160$ a, as indicated. Note that the L fraction has been multiplied by a factor of 2 so that the patterns are easily visible with the same color bar.

4.2. Transit Time Distributions and Ideal Mean Age

[43] A convenient summary of the temporal information contained in the boundary propagator is the distribution of transit times since last surface contact regardless of where on the surface that contact occurred. We will refer to this as the global transit time distribution (TTD) obtained as

$$g(\tau_n|\mathbf{r}, m_0) \equiv \sum_m \sum_s \mathcal{P}(s, m, n|\mathbf{r}, m_0), \qquad (13)$$

where m is summed to average over the seasonal cycle, and $\tau_n = n$ is the number of years since last surface contact.

[44] Figure 8 shows these TTDs at the bottle depths for the profiles at 39.9°N and 20.8°N, and for each of the four inversion cases considered. The profile at 39.9°N passes through the region of highest L + N water mass fractions of age less than ~40 a, while the profile at 20.8°N passes through the region of highest L + N fractions of age older than ~40 a as identified by the inversion using the AD prior with CFC-11 (Figure 6). We note that below the thermocline the patterns of Figure 6 show that section A20 is least ventilated at ~20°N, consistent with the CFC minimum there between ~1 and ~2 km depth.

[45] Figure 8 shows that in the case of the uniform prior without CFC-11 the TTDs decay monotonically from a nonzero value at $\tau = 0$ because the time dependence comes solely from the radioactive decay of ^{14}C, which results in the functional form $\propto \exp[-\lambda_j C_j^S \exp(-\gamma_j \tau)]$. (Note that this is not simply exponential decay, and that for this function to converge to zero for increasing τ, the Lagrange multiplier for ^{14}C must be negative.) The short-time dependence of these TTDs is clearly unphysical; very little surface water should reach the deep in the first year so that the TTDs are expected to start off at a value near zero. Including CFC-11 with the uniform prior improves the results dramatically by adding additional constraints for the first ~75 a of transit

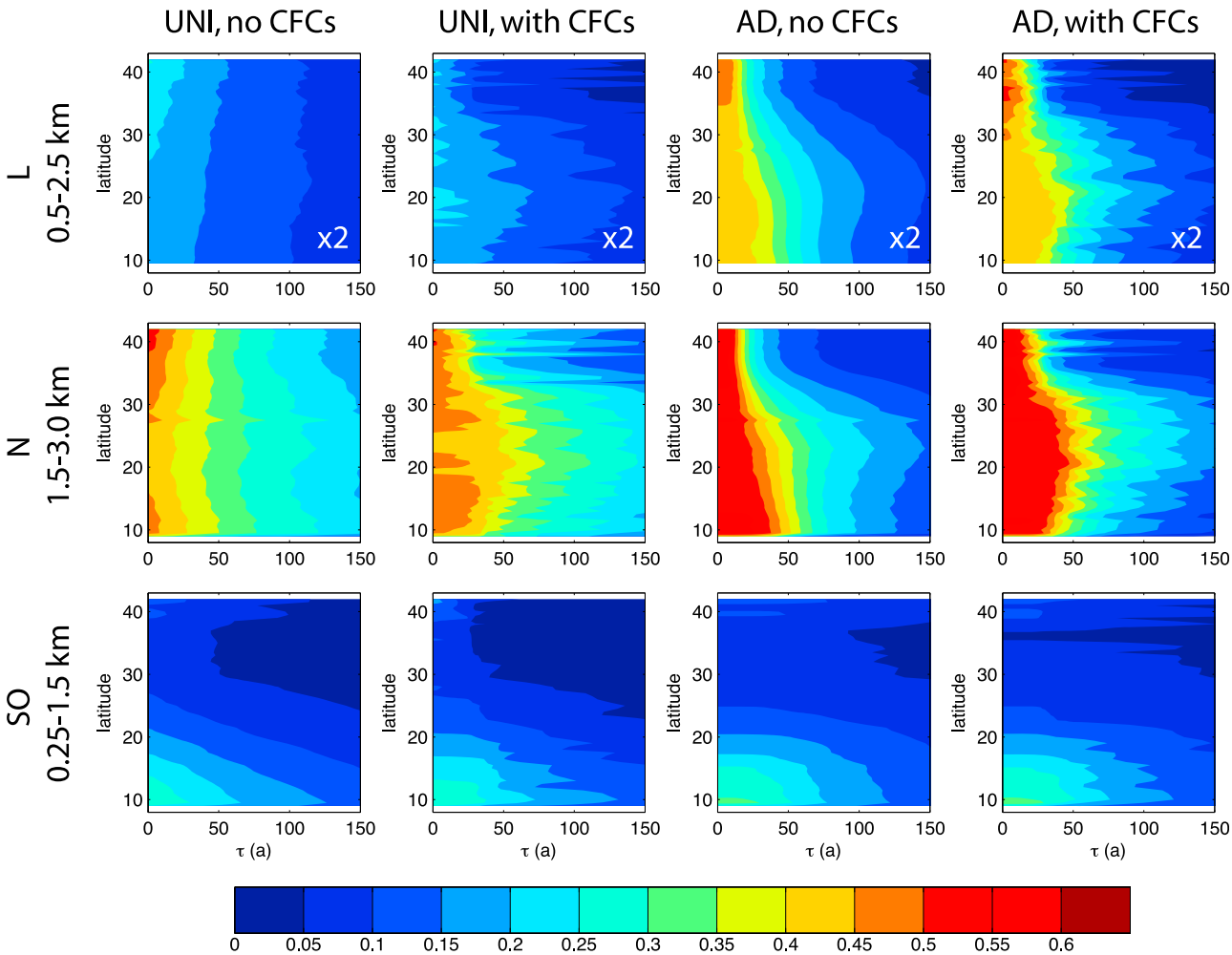

Figure 7. The fraction of (top) L, (middle) N, and (bottom) SO waters of age τ or older as a function of τ, averaged over vertical slabs as indicated. The L fraction was multiplied by a factor of 2 as in Figure 6.

time. The 1997 and 2003 CFC-11 values add two more degrees of freedom to the functional form of the ME solution (8), allowing the TTDs to deviate from the ^{14}C tails. For most (but not all) depths the CFCs are able to drive the TTDs close to zero in the first year. The fact that the early part of the TTDs deconvolved with CFC-11 at 20.8°N is driven to zero at most up to ~75 a for any depth is due to the fact that beyond ~75 a the time dependence comes only from ^{14}C.

[46] Even for the case of the AD prior, Figure 8 shows that the inclusion of CFC-11 is important for the shape of the TTDs at early times. Further partitioning of $g(\tau)$ (by summing $\mathcal{P}$ only over select regions, not shown) reveals that the early mode for the no-CFC case comes from water last ventilated in the Mediterranean. However, inclusion of CFC-11 removes this feature except for the very small blips visible in the 20.8°N distributions for $\tau_n < 20$ a between 1000 and 2000 m depths. (The sharper blips visible below 3500 m in the 39.9°N distributions for $\tau_n < 20$ a are due to Nordic/Barents Sea Water.) Overall, the TTDs again show the pattern of young water in the northern part of the section, with older waters in the southern part that we described in terms of water mass fractions.

[47] The ideal mean age, Γ, is the expected value of the time $\tau_{n,m}$ since last contact with the surface anywhere, and hence obtained as

$$\Gamma(\mathbf{r}, m_0) \equiv \sum_{m,n,s} \tau_{m,n} \mathcal{P}(s, m, n|\mathbf{r}, m_0). \tag{14}$$

The ideal mean age is shown in Figure 9 for our four inversion cases. For all cases the pattern of Γ is broadly similar, but using the AD prior produces larger mean ages throughout. For the uniform prior the AAIW tongue is reflected in a tongue of locally older water, and inclusion of CFC-11 reduces mean age in the vicinity of the northern middepth CFC plume consistent with our picture from the water mass fractions.

5. Uncertainty Estimation

[48] Our ME deconvolutions for $\mathcal{G}$ must contend with three sources of uncertainty.

[49] 1. The tracer data itself has uncertainty primarily due to the sparse spatial and temporal sampling of the surface boundary conditions. We ignore instrumental error here as it is negligible compared to the other sources.

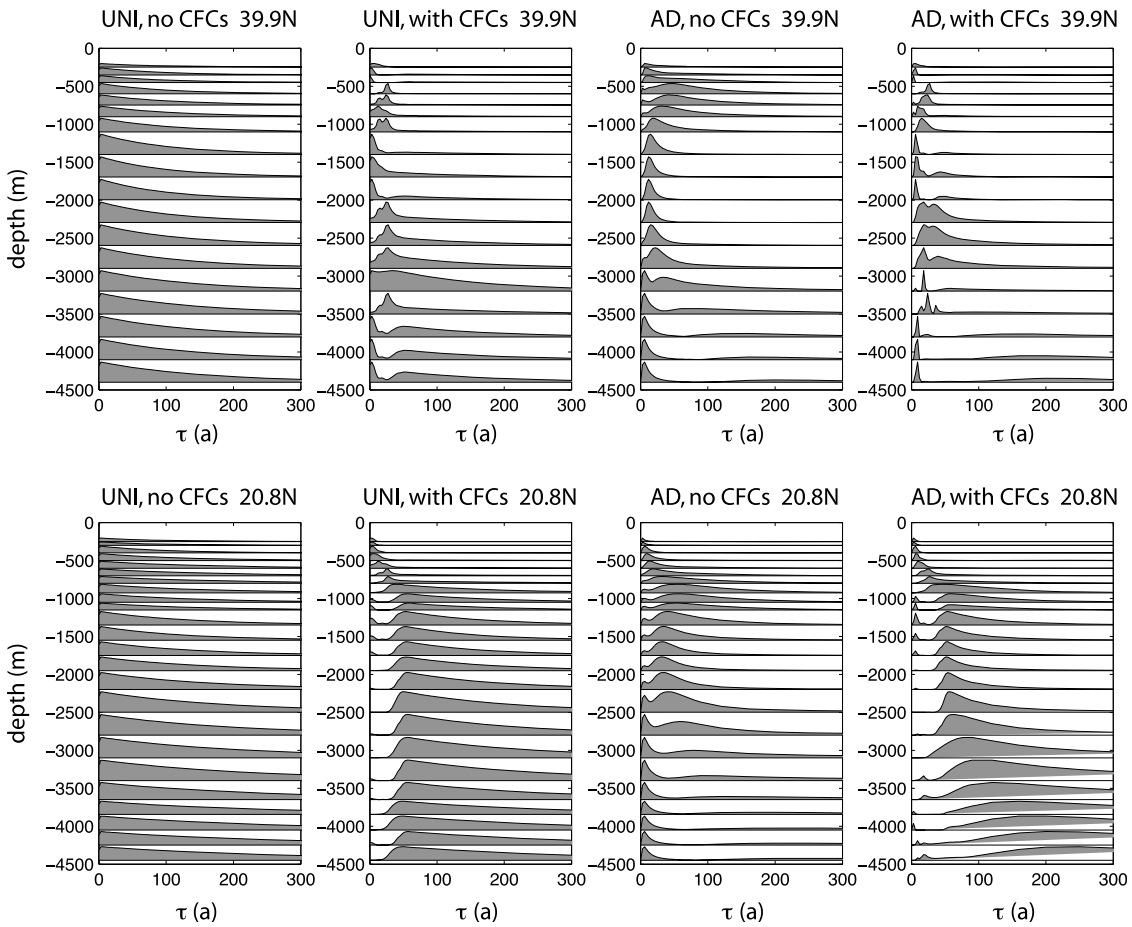

Figure 8. The seasonally averaged distribution of times τ since last contact with the surface anywhere for the A20 profiles indicated and for the cases of uniform (UNI) and AD prior, with and without CFC-11. For plotting, the distributions have been normalized by their maximum value and scaled to fit the space between adjacent depths.

[50] 2. There is "model error" arising from the assumptions built into the conceptual model underlying our analysis. Specifically, there will be errors due to our assumptions of cyclostationary flow with no temporal eddy variability, no interannual variability, and perfect PO_4^* conservation.

[51] 3. There is also significant uncertainty due to missing information, termed "entropic uncertainty" here, which can be quantified using the information entropy. Even if we had perfect data, the flow was perfectly cyclostationary, and PO_4^* was perfectly conserved, we would still not be able to reconstruct $\mathcal{G}$ with certainty. The available tracers provide far too little information to constrain the rich information of $\mathcal{G}$ with precision. We therefore begin with the entropic errors, which tend to dominate.

5.1. Method of Uncertainty Analysis

[52] We would like to know the probability distribution of a diagnostic $\hat{D}[\mathcal{P}]$ that can be obtained as $\hat{D}[P] = \sum_{s,m,n}\mathcal{P}(s, n, m|\mathbf{r}, m_0)\, F(s, n, m)$ for a suitable function $F(s, n, m)$. One example is water mass fraction $\hat{D} = f$, where F is a spatial mask for the surface index s independent of n, m; another example is mean transit time $\hat{D} = \Gamma$, for which $F = \tau_{n,m}$, independent of s.

[53] The probability density of diagnostic $\hat{D}$ taking a particular value $D \in (D, D + dD)$ is given from equation (6) by

$$p(D) \propto \exp\left(-\frac{N}{2}\frac{\mathcal{S}(D)}{\mathcal{S}(D^*)}\right), \tag{15}$$

with the additional constraint that $D = \hat{D}[\mathcal{P}]$, which we implement here by adding the Lagrange multiplier term $\lambda_D(D - \hat{D})$ to the data constraints in equation (2). In (15) D^* is the value of D for $\lambda_D = 0$, that is, the value of D without the additional constraint. We take $N = J$, the number of tracer constraints used. Thus, $N = 6$ when we use CFC-11 for both 1997 and 2003, θ, S, PO_4^*, and ^{14}C, and $N = 4$ when CFC-11 is not used. Equating N with the number of constraints [e.g., *Gull and Daniell*, 1978] is the choice of the so-called "classic" maximum entropy method [e.g., *Skilling and Gull*, 1991]. In later refinements by *Skilling and Gull* [1991] it is argued that N should be the number of linearly independent constraints on $\mathcal{P}$. Given that the tracers we use all have very different boundary conditions, we can reasonably expect our $N = J$ constraints to be linearly independent. Note, however, that if one were to include tracers with very similar boundary conditions such as CFC-11

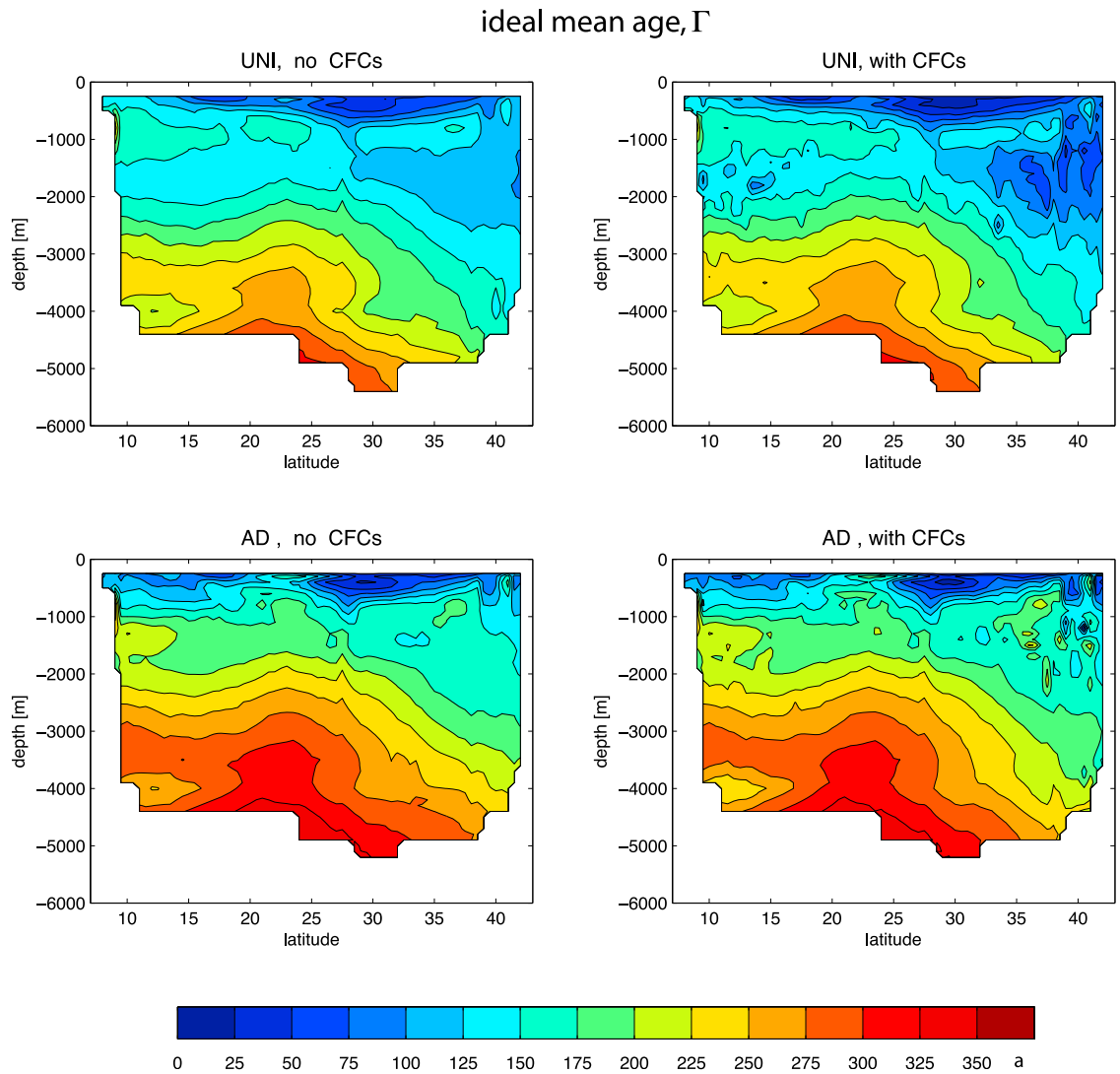

Figure 9. The distribution of the ideal mean age, Γ, or equivalently, the mean time since last surface contact, for section A20. The cases of uniform (UNI) and AD priors with and without CFC-11 are shown.

and CFC-12, the number of independent constraints would likely be less than J.

[54] Finding $p(D)$ requires solving $J + 1$ nonlinear equations for the Lagrange multipliers for each value of D. Hence, tracing out the pdf $p(D)$ over a reasonable range of D is computationally expensive. We therefore compute the entropy $\mathcal{S}(D)$ only at two values of D on each side of the ME value of D^* and use these points to fit $\mathcal{S}$ to a power law $\mathcal{S} = b|D - D^*|^a$ separately on each side of the maximum. Typically $a \sim 2$ so that we are fitting the multiplicity term $\exp(\alpha\mathcal{S})$ to an asymmetrically stretched or compressed Gaussian. We verified that this is a reasonable approximation for a few cases and accept modest inaccuracies incurred because we are using the multiplicity only to infer uncertainty.

[55] We assign error bars for diagnostic D based on our approximation of $p(D)$ as follows. A quartile error bar captures the left and right quartiles of $p(D)$ and a half-width error bar stretches from the left to the right half-peak value of $p(D)$. When D is positive definite, as is the case for water mass fractions and mean age, less than one quartile may lie to the left of the mode. In this case, the quartile error bar starts at the distribution's leftmost percentile and covers half the probability of finding D. (In all cases an integral of our estimate of $p(D)$ over the quartile error bar yields a probability of 0.5.)

[56] The entropic uncertainty is of course not the only source of uncertainty. The measured or inferred surface boundary conditions and interior tracer values also carry uncertainty, primarily due to data sparsity for the boundary conditions and mesoscale variability for the interior values. To deal with these uncertainties, we assume that the data are one particular realization drawn from a multivariate Gaussian probability distribution whose covariance structure is estimated from the data uncertainties as described in Appendix B. In particular, the local bottle values of CFC-11 are subject to mesoscale variability, while the smoother gridded data is more representative of climatology. This mismatch results in some degree of inconsistency between the surface boundary conditions and the interior data. To account for this, we take the interannual variability of CFC-11 around its secular trend as the uncertainty of the CFC-11 data for our Monte

Carlo uncertainty estimates. This variability was estimated from the relatively frequently sampled line W (Figure 1) hydrography (see Appendix B).

[57] The effect of the data uncertainties on our inversions can then be quantified by the following Monte Carlo integration: random realizations of the boundary conditions and the interior tracer values are drawn from the data's assumed probability distribution. In principle we would now like to compute $p(D)$ for each such realization and then integrate (essentially average) all of the resulting distributions. To save computational expense we instead assume that the shape of $p(D)$ does not change appreciably with each realization, so that the only change in $p(D)$ is a simple shift in its mode D^* (the value of D for which $p(D)$ is at its maximum) to the ME value D_0 for each realization. Thus, if $p_E(D_0)$ is the distribution of the ME values of D obtained by binning the ME values from an ensemble of data realizations, our data uncertainty corrected probability distribution $p_C(D)$ is given by the convolution

$$p_C(D) = \int dD_0\, p_E(D_0)\, p(D - D_0 + D^*). \tag{16}$$

Because even this approximate Monte Carlo estimation is computationally intensive (we used ensembles of ~100 realizations), we only examined the data-corrected uncertainty for a few bottles. This is justifiable because the highly underconstrained nature of the problem typically results in broad distributions $p(D)$. The data uncertainties typically only lead to modest additional broadening.

5.2. Uncertainties of the Water Mass Fractions

[58] The entropic uncertainties of the mass fractions $f_R(\tau|\mathbf{r}, m_0)$ at 39.9°N are shown in Figure 10 for both the uniform and AD priors with CFC-11. Figure 10 shows that there is substantial entropic uncertainty in the water mass fractions. This should come as no surprise given the hugely underdetermined nature of the deconvolutions. Conditioning on minimum transit time (the fractions with $\tau \geq 39$ and 160 a), does not significantly increase the uncertainties for the L and N fractions in spite of the fact that specifying a transit time threshold demands more detailed information from the inversions. (Exceptions are the global (G) fractions of age τ or older (regardless of where contact occurred, last column of plots), whose uncertainty increases with increasing τ from a trivially certain value of unity at $\tau = 0$.) The uncertainty in the global fraction with $\tau \geq 160$ a is comparable to the uncertainty of the N and N + L fractions. The smallest absolute uncertainties are seen for the SO fractions, indicating that the available tracers provide relatively strong constraints on f_{SO}.

[59] The comparison between the uniform and AD prior inversions of Figure 10 shows that measuring information relative to the AD solution shifts the most likely values (the red diamond ME values). In spite of this shift, the uniform and AD prior solutions are consistent with each other in the sense that their error bars overlap. The additional transport information provided by the AD prior significantly reduces the entropic uncertainty compared to the uniform prior case except below ~3.5 km, where the error bars are similar. The AD prior quartile error bars are up to a factor of ~3 smaller than in the corresponding uniform prior case. However, even with the AD prior the uncertainties are generally still quite large, which means that even relative to the AD prior, there is still a large multiplicity of possible solutions consistent with the data constraints. We will now examine the more subtle case of the ideal mean age, for which inconsistencies between the priors and $\Delta^{14}C$ conspire to produce large entropic uncertainties even in the case of the AD prior.

5.3. Uncertainties of the Ideal Mean Age

[60] Figure 11 shows the entropic uncertainties of the ideal mean age, Γ, for the profile at latitude 39.9°N for all four inversion cases. The uncertainties are substantial, but all four cases are consistent with each other in the sense that their error bars overlap. For the uniform prior CFC-11 helps to reduce the uncertainty in Γ where CFC concentrations are relatively high between ~1 and ~2 km depth.

[61] For a number of bottles the error bars of Γ in the case of the AD prior are about as large as, or even larger than, the corresponding error bars in the case of the uniform prior, particularly when CFC-11 is included in the inversions. This is at first surprising because the AD prior provides nontrivial transport information, which in the case of the water mass fractions was seen to lead to substantial reductions in the error bars (Figure 10). However, Γ is sensitive to the tails of the TTD, and the tails of the deconvolved boundary propagator tend to be more sensitive to inconsistencies between the AD prior and the available tracer data than is the case for the uniform prior. The mathematical mechanism is the following: the AD prior tends to be too young in the upper ~2.5 km compared to what is expected from the depletion of ^{14}C. (The uniform prior is too old with Γ = 2000 a everywhere). In the AD case, therefore, the maximum entropy solution places more weight into the tail of the TTDs by switching the sign of the ^{14}C Lagrange multiplier to positive. The exponentiated surface history term $\propto \exp[-\lambda_j C_j^S \exp(-\gamma_j \tau)]$ then increases with increasing τ, while the multiplicative prior μ ensures that $\mathcal{P}$ still eventually decays to zero. This extra weight in the tail has little visible effect on the global TTD, but when the TTD is multiplied by the transit time this extra weight causes a considerable bulge in the integrand for Γ beyond 4000 a. While the integrand $\tau_{n,m}\mathcal{P}$ still has sufficient weight at smaller transit times to yield reasonable mean ages, in regions of positive ^{14}C Lagrange multipliers, transit times longer than 4000 a contribute significantly to Γ. For the AD prior with CFC-11, in the region of the northern middepth CFC plume the contribution to Γ from waters older than 4000 a can be about twice the contribution from waters younger than 4000 a, and in the older regions of the upper ocean visible in Figure 9, these contributions can be even higher (to about an order of magnitude). We emphasize that these are contributions to mean age from very old waters; the water mass fractions older than 4000 a themselves are very small. (The water mass fraction older than 4000 a is at most between 1% and 2% for 3.7% of the bottles, and for 80% of the bottles this fraction is less than 0.1%.) For the uniform prior, contributions to mean age from transit times beyond 4000 a are ruled out a priori, removing some of the sensitivity of mean age to inconsistencies between prior and data. Because the uniform prior is too old compared to the ^{14}C depletion, the ^{14}C Lagrange multiplier is always positive

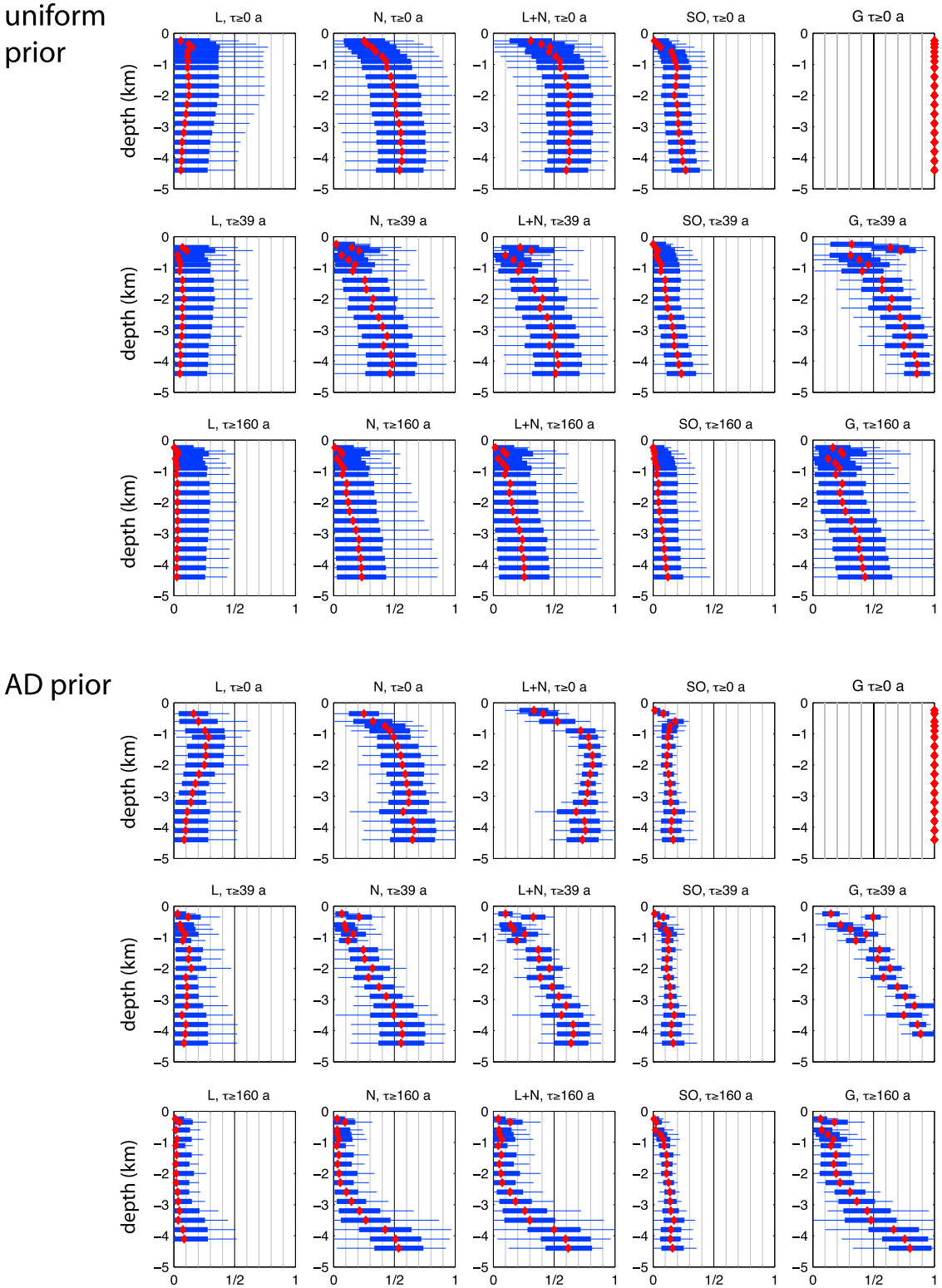

Figure 10. Estimate of the entropic error in the water mass fractions of age τ or older for the profile at 39.9°N and the values of τ indicated. Results for the uniform and AD priors are shown, as indicated (both with CFC-11). For each depth, a red diamond locates the ME value. Quartile (thick) and half-width (thin) error bars were determined as described in section 5.

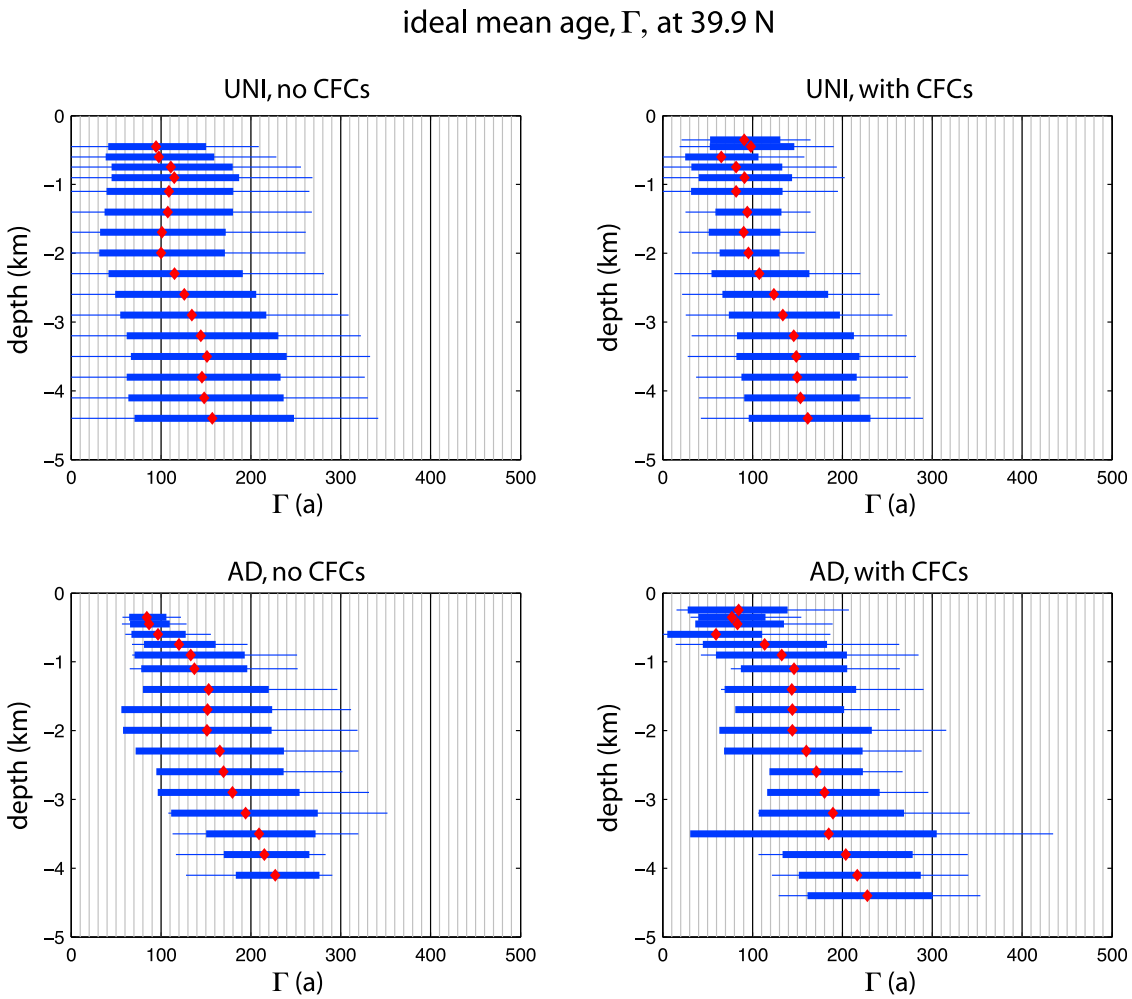

Figure 11. Estimate of the entropic error in ideal mean age, Γ, for the profile at 39.9°N. The cases of uniform (UNI) and AD priors with and without CFC-11 are shown. For each depth, a red diamond locates the ME value. Quartile (thick) and half-width (thin) error bars were determined as described in section 5.

and the integrand $\tau_{n,m}\mathcal{P}$ has typically decayed to near zero by 4000 a.

[62] The large error bars of Γ show that a considerable range of TTDs with differing first moments can be accommodated while still satisfying the tracer data. In this sense mean age is not a robust diagnostic. None of the tracers used directly constrains the first moment of the globally surface-integrated boundary propagator (13), that is, none of the tracers has linear time dependence and spatially uniform boundary conditions. While radiocarbon, because of its nearly linear decay over the temporal evolution of the TTDs in the North Atlantic, does provide information on mean age, the spatial variations in the ^{14}C surface concentration contribute significantly to the uncertainty of Γ as we will now explore by comparing radiocarbon age to ideal mean age.

[63] The radiocarbon age, Γ_C, is defined by $\Gamma_C(\mathbf{r}) = \gamma^{-1} \ln [C_0(\mathbf{r})/C(\mathbf{r})]$, where $C_0(\mathbf{r}) = \sum_s f(s|\mathbf{r})C(s)$ is the "initial" ^{14}C concentration (in the terminology of *Broecker and Peng* [2000]), with $f(s|\mathbf{r}) \equiv f(s, 0|\mathbf{r}, m_0)$ being the water mass fraction at $\mathbf{r}$ that was last ventilated at surface box s (see equation (12)). The concentration $C_0(\mathbf{r})$ is the concentration one would have in the absence of radioactive decay so that comparison with the observed decay defines $\Gamma_C(\mathbf{r})$. It can be shown [e.g., *Deleersnijder et al.*, 2001; *Hall et al.*, 2002; *Waugh et al.*, 2003] that for the case of spatially uniform boundary conditions and a TTD whose width is small compared to the radiocarbon decay time, Γ_C and Γ should be the same to a good approximation. For real natural radiocarbon, the surface concentration varies across the globe with Δ^{14}C ~ −40 per mil in the subtropical gyres to Δ^{14}C ~ −135 per mil in the Southern Ocean and accurate determination of Γ_C requires accurate determination of $C_0(\mathbf{r})$. In Appendix D we work out the conditions for which Γ_C should approximate Γ for the case where the surface boundary condition for radiocarbon varies spatially: terms that would vanish for spatially uniform boundary conditions must be small compared to unity.

[64] Because we can compute $C_0(\mathbf{r})$ exactly for a given ME estimate of the boundary propagator, we can quantify to what extent Γ_C approximates Γ across section A20. To that end, Figure 12 shows the percent difference between Γ_C and Γ for our four inversion cases. When the AD prior is used with CFC constraints $\Gamma_C \sim \Gamma$ to a good approximation (5% to 10% over most of the section). For the other cases, the differences between Γ_C and Γ are more substantial, which

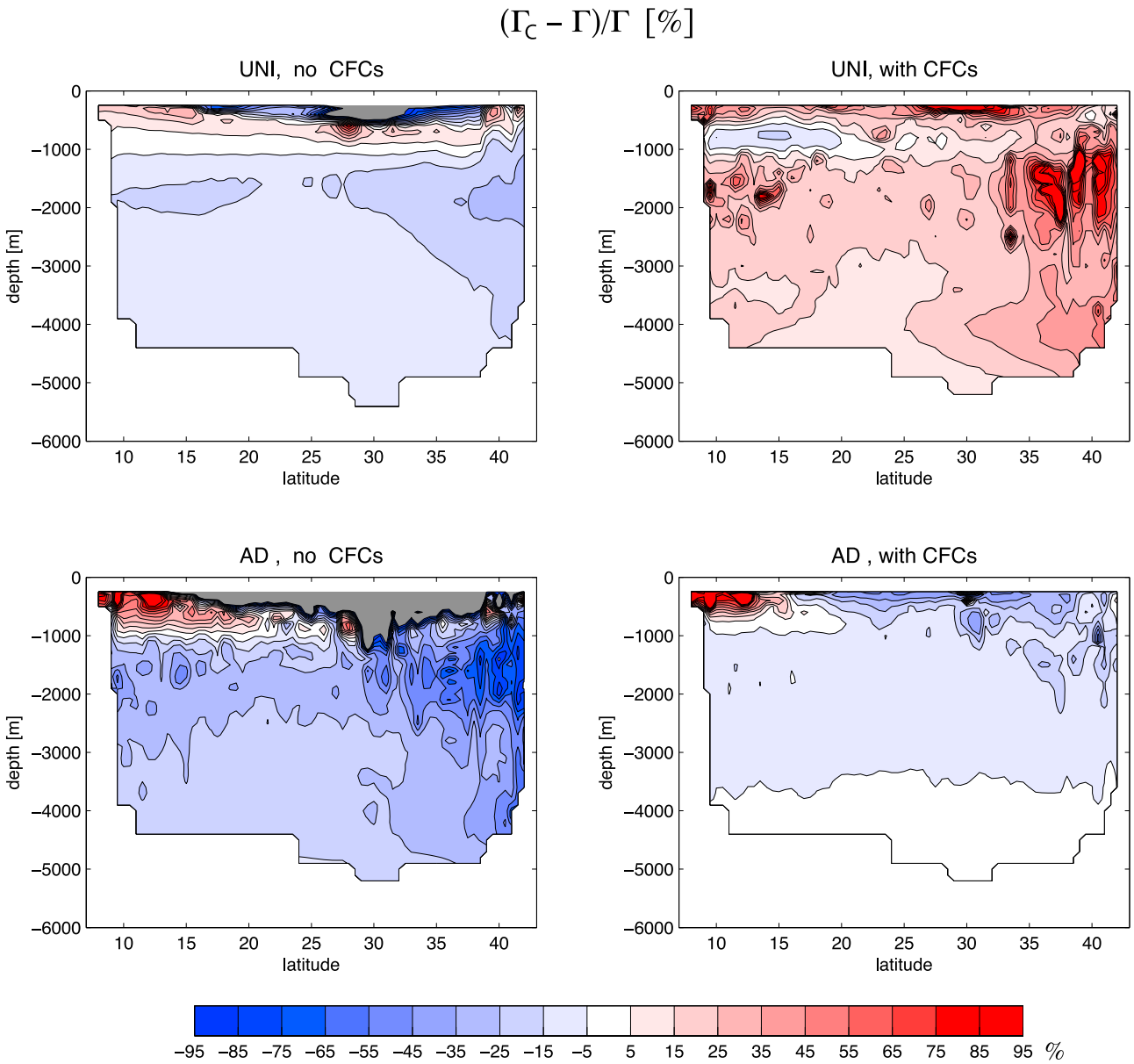

Figure 12. The percentage difference between radiocarbon age, Γ_C, and ideal mean age, Γ, across section A20. The cases of uniform (UNI) and AD priors with and without CFC-11 are shown. In the grey regions near the surface for the no-CFC cases, the radiocarbon age is undefined because the interior concentration $C(\mathbf{r})$ is larger than the estimate of the initial concentration $C_0(\mathbf{r})$.

means that the correction terms of Appendix D cannot be neglected. When CFCs are not used in the inversions, the initial radiocarbon concentration $C_0(\mathbf{r})$ is unphysically larger near the surface than the actual concentration $C(\mathbf{r})$, leading to an undefined radiocarbon age there (the grey areas of Figure 12). The fact that the discrepancy between Γ_C and Γ depends on the inversion case underlines the sensitivity of age to the detailed dependence of the boundary propagator on both transit time and surface origin. It is important to emphasize that even when the ^{14}C age is a good approximation to ideal mean age, one cannot conclude that either is known with certainty, only that the uncertainty in the two ages must be equal.

[65] A key advantage of the ME approach is that it allows us to determine the uncertainty of the ideal mean age associated with the underdeterminedness of the deconvolution. Purely within the framework of the radiocarbon age this uncertainty is hidden from view and subsumed primarily into the uncertainties of the water mass fractions $f(s|\mathbf{r})$, which come into play because of the spatial variations in the surface ^{14}C concentrations (see Appendix D). If the surface ^{14}C concentration was uniform, the uncertainties in $f(s|\mathbf{r})$ would not affect Γ_C, and, to the extent that $\Gamma_C \simeq \Gamma$, our estimate of the uncertainties of the ideal mean age would be much lower. From the point of view of the TTD, which is $\mathcal{G}$ globally integrated over surface origin (equation (13)), the

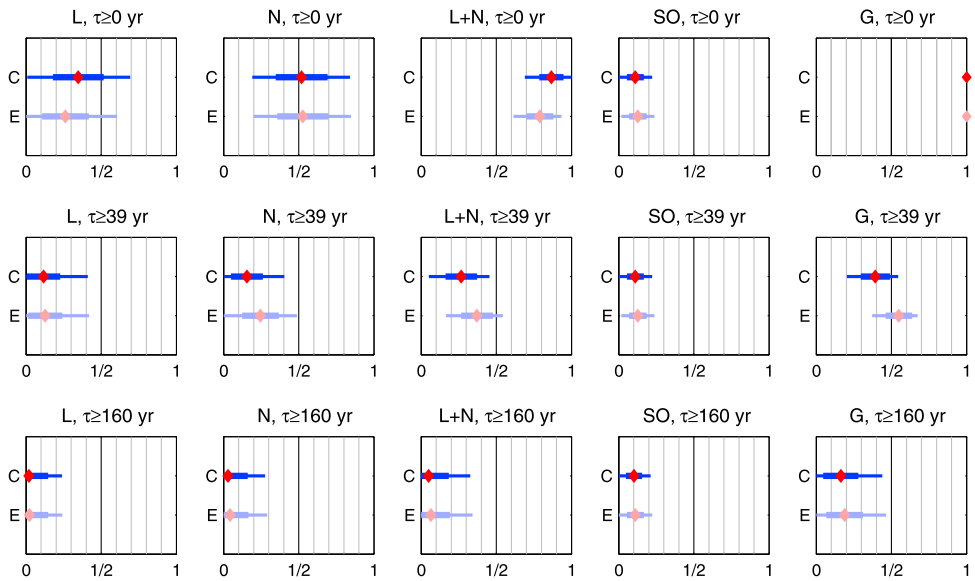

Figure 13. The effect of data error on the uncertainty of the water mass fractions of age τ or older for the values of τ indicated at latitude 39.9°N and 1.40 km depth for the deconvolutions with the AD prior including CFC-11. The purely entropic error bars are labeled E (faded colors), and the error bars with corrections from data uncertainties are labeled C. In each case, a red diamond locates the most likely value.

uncertainty in surface origin renders the functional form of the TTD sufficiently uncertain to admit a range of first moments as evidenced by the large entropic uncertainty in mean age.

5.4. Effect of Data Uncertainties

[66] Figure 13 shows the effect of the data uncertainties for the water mass fractions at a single location (1.40 km depth, 39.9°N). The increase in the size of the width-at-half-maximum error bars from the purely entropic, zero-data-uncertainty case (labeled E in Figure 13) to the data uncertainty-corrected case (labeled C) is at most ~7% and barely visible in Figure 13. (If both entropic and data errors were Gaussian, a 7% increase in the width at half maximum would result from the data errors having 38% of the standard deviation of the entropic errors.)

[67] Interestingly, inclusion of the data uncertainties can shift the mode (the most likely value, indicated in Figure 13 by a red diamond) of the distribution from its value in the purely entropic case (e.g., the horizontal shift in the mode and error bars from their purely entropic values (case E) to their values with the data uncertainties (case C) for L + N, $\tau \geq 0$ and N, L + N, and G for $\tau \geq 39$ a). These shifts give an indication of the degree to which the maximum of $\alpha\mathcal{S} - \chi^2/2$ can be approximated by the maximum of $\mathcal{S}$ subject to zero-misfit data constraints. However, because the purely entropic error bars are very broad, the shifts occur within the entropic error range. We therefore did not deem the considerable computational expense of quantifying mode and error more accurately worthwhile for this study.

[68] We note in passing that noise-induced shifts in the mode of the distribution are not a peculiarity of the maximum entropy deconvolution. For example, very similar effects can be obtained in simple deterministic matrix inversions for three water masses using two tracers and the constraint that the fractions sum to unity. Gaussian perturbations of the interior and surface tracer values can lead to distributions of the fractions with modes that are different from the noise-free solution when the variances of the interior and surface values are well separated. A detailed investigation of this effect is, however, beyond the scope of this study.

5.5. Discussion

[69] Before summarizing our key findings it is important to keep in mind the assumptions, approximations, and inherent limitations of our analysis.

[70] 1. Cyclostationary flow is only a rough approximation necessitated by the temporally sparse tracer data. The real ocean is filled with mesoscale eddies and will also have interannual and longer timescale variability. Although we have included estimates of temporal variability in our uncertainty analysis, any allowance for variability or secular changes, such as may result from climate change, in the boundary propagator itself is absent from our ME inversions as currently formulated.

[71] 2. There is no annual cycle for the CFC mixed layer concentrations, or equivalently, no annual cycle in the CFC saturation. This is clearly unrealistic. For example, convectively driven ventilation tends to occur predominantly in late spring, so that in key water mass formation regions the CFC mixed layer concentration is likely to have an annual cycle with pronounced peaks [e.g., *Stommel*, 1979; *Haine and Richards*, 1995; *Williams et al.*, 1995]. Smoothing this to annual means (which are linearly interpolated from month to month) and assuming constant saturation are merely expedient approximations in the face of insufficient data (see *Huhn et al.* [2008] for an approach to deal with changing saturation). Given the substantial entropic uncertainties, we did not attempt to bound the effect of these approximations. Estimating CFC boundary conditions with

realistic seasonality from the available data is an important direction for future research.

[72] It is also important to keep in mind inherent limitations of the ME method as implemented here. Other than the information provided by the prior, μ, our ME inversions are blind to the circulation and global basin geometry. Furthermore, our ME inversions operate only on the local tracer data at ($\mathbf{r}$, t). The information contained in tracer gradients and the path information encoded in the structure of the CFC plume are not exploited. Thus, for the case of the uniform prior any path length information is entirely absent. The surface of the Southern Ocean is treated on the same footing as the nearby Atlantic surface. This results in unphysical artifacts. Specifically, the water mass fractions from different regions of the world ocean have a transit time distribution with a common mode. In other words, regardless of whether the fraction of Southern Ocean or nearby Atlantic waters is considered, the largest water mass fraction of age $\tau \in (\tau, \tau + d\tau)$ occurs at nearly the same τ. This unphysical feature provides a strong argument for the use of an advective-diffusive (or other) prior that encodes some physical information on transport paths and/or basin geometry.

[73] With only three Lagrange multipliers associated with transient tracers, our ME inversions' ability to shape the temporal structure of the boundary propagator is limited. In particular, for transit times older than ~75 a, time information is provided only by ^{14}C (which also highlights the importance of quality data for natural ^{14}C). For the uniform prior, this limitation means that transit time distributions are unable to form a mode (peak) for ages older than ~75 a. However, it is worth pointing out that the ME inversions presented here still have much greater flexibility in shaping TTDs than parametric TTD methods that assume a single dominant end-member and a one- or two-parameter inverse Gaussian functional form from the outset [*Hall et al.*, 2002].

[74] To quantify the ME-deconvolved boundary propagator's ability to predict tracers that were not used as constraints, we consider CFC-12. Because CFC-11 and CFC-12 have similar time histories, we expect prediction errors for CFC-12 to be small for the cases where CFC-11 constraints were used in the ME inversions. Figure 14 shows predictions of CFC-12 across section A20 for the four inversion cases together with the observed CFC-12 distribution and its discrepancy with the AD-with-CFC-11 case. The necessary boundary conditions for CFC-12 were prepared in the same fashion as those for CFC-11 (see section 3.1). The ME deconvolution with a uniform prior but no CFC-11 results in a boundary propagator that does not capture the early-time (τ < 75 a) transport and grossly underpredicts CFC-12. Using the AD prior without CFC-11 results in a boundary propagator that predicts CFC-12 only in very broad strokes: there is a middepth maximum in the northern half of the section, but it is too broad and smooth, and the surface CFC-12 maximum is too shallow and weak. The broadness of the predicted CFC-12 is a direct consequence of the broadness of the AD prior itself, which was deliberately broadened with respect to surface origin so as not to exclude any water mass formation regions merely by choice of prior.

[75] When the CFC-11 constraint is enforced in the ME deconvolutions, the predicted CFC-12 distribution is nearly identical for the uniform and AD priors. The difference between predicted and observed CFC-12 shows that the CFC-11-constrained $\mathcal{G}$ tends to underpredict CFC-12 by 5%–10%. The magnitude of this mismatch is on the same order as the eddy variability of the CFC-12 data (see Appendix B), and the systematic underprediction points to $\mathcal{G}$ having insufficient young water. The relatively small discrepancy between predicted and observed CFC-12 nevertheless demonstrates that the part of $\mathcal{G}$ necessary to propagate tracers with a surface history that is similar to that of CFC-11, such as CFC-12, has been well constrained by CFC-11 and the other tracers used in the inversion regardless of choice of prior. This also bodes well for using CFC-11 constrained boundary propagators for propagating anthropogenic carbon dioxide [*Khatiwala et al.*, 2009], whose surface history is similar to that of the CFCs.

[76] These assumptions and limitations, as well as the substantial entropic uncertainties, emphasize the importance of not overinterpreting our inversions for the boundary propagator. With the available data it is impossible to capture all of the richness of the boundary propagator in detail. We have therefore limited our analysis to a few key diagnostics, with the water mass fractions of age τ or older being particularly robust.

6. Summary and Conclusions

[77] We used maximum entropy (ME) deconvolutions to partition the water along WOCE line A20 according to where and when it was last in the mixed layer. The entropy itself was then used to estimate the uncertainty of the inversions due to the underdetermined nature of the deconvolutions, and a Monte Carlo method was explored to estimate the additional effects of the data uncertainties. Our key findings are as follows.

[78] 1. The ME inversions objectively identify both Labrador/Irminger Sea Water (L water) and overflow waters that were last ventilated in the Nordic/Barents seas (N water). The deconvolved joint probability of times and locations of last surface contact (the boundary propagator) was then integrated to quantify the mass fraction of these waters of age τ or older as a function of τ. The bulk of the L and N fractions is less than ~40 a old in the vicinity of the DWBC at the northern end of A20 but several decades older where the DWBC recrosses the section further south. This lag in propagation time is much longer than the DWBC's advective timescale of a few years and points to the importance of mixing via a multitude of eddy-diffusive paths. This picture of a diffusive conveyor [*Holzer and Primeau*, 2006, 2008] is also supported by the fact that the L and N fractions are distributed over a much broader range of transit times in the southern part of the section than in the northern part. Section A20 contains little L water older than ~160 a. The overflow waters lie primarily below the L waters and include water as old as ~600 a below ~3500 m.

[79] 2. Estimates with the uniform and AD priors have overlapping error bars and are therefore consistent with each other. For the inversions with the uniform prior it is essential to include CFC-11 data to capture the structure of the water mass fractions for transit times $\tau \lesssim 75$ a). When the ME inversion is constrained by CFC-11, the early part of the boundary propagator (τ < 75 a) is insensitive to the choice of prior, as evidenced by the fact that the ME-derived

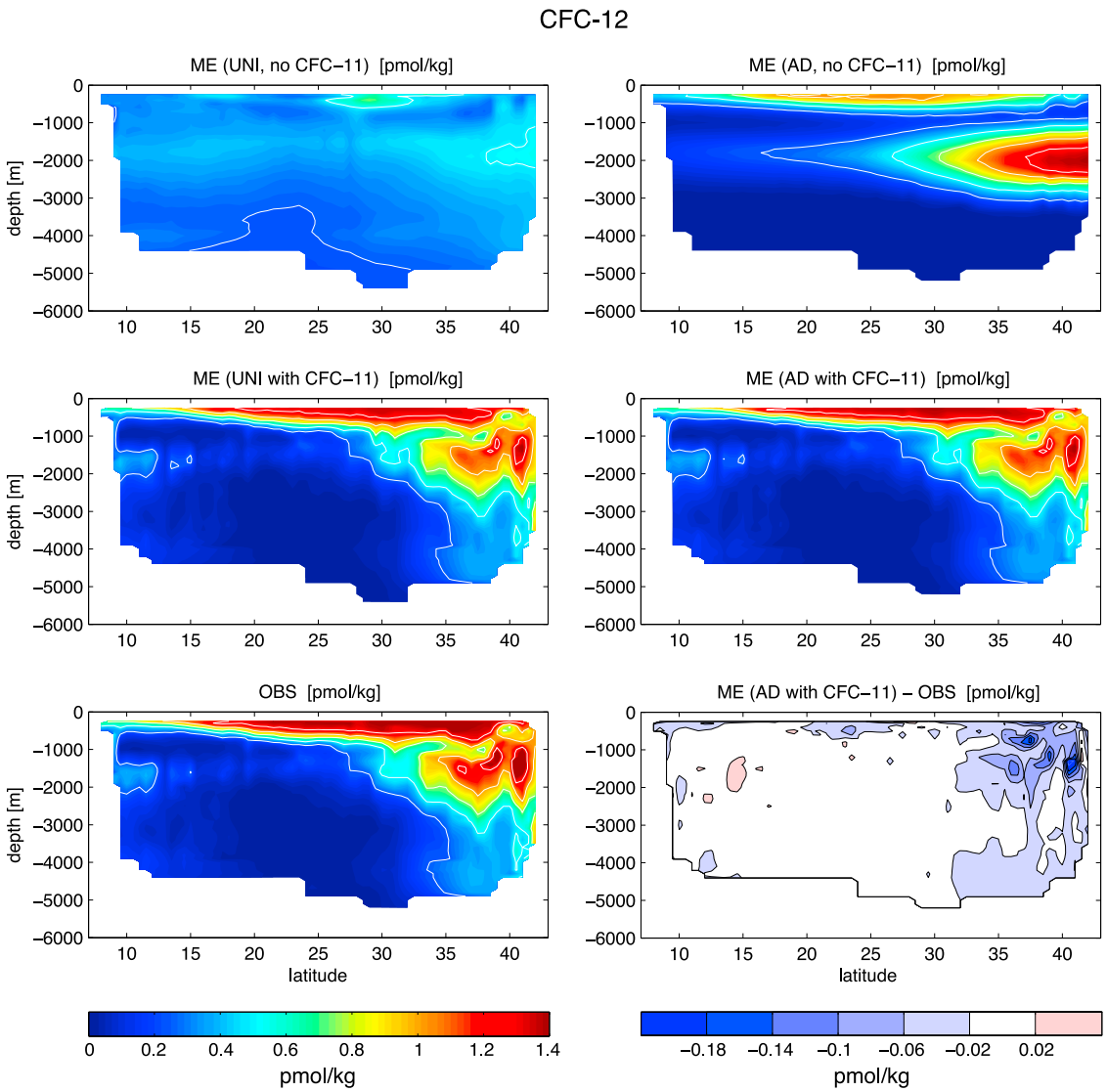

Figure 14. The first four plots show the concentration of CFC-12 across section A20 as predicted by the ME-deconvolved boundary propagator for the four inversion cases. The last two plots show (right) the observed CFC-12 concentration and (left) the difference between the prediction for the AD-with-CFC-11 case and the observations. For all plots, only those bottles for which both the 1997 and 2003 CFC-11 values could be used in the deconvolution were considered. The white contours for the CFC-12 concentration have an interval of 0.25 pmol/kg.

boundary propagator gives nearly identical predictions for CFC-12, which was not used as a constraint, regardless of whether the uniform or AD prior is used.

[80] 3. The entropic uncertainties of the water mass fractions are substantial, with the quartile limits of their probability distributions nearly spanning a water mass fraction as large as 0.5 for the worst cases of the inversions with the uniform prior. Use of the AD prior significantly decreases the uncertainties of the water mass fractions by providing prior transport information to the inversions. The uncertainties of the water mass fractions older than a given threshold age do not systematically increase with the threshold age, except in the case of the global fraction, which trivially reduces to exactly unity when all ages are included. The entropic uncertainties capture the physical fact that a large number of possible locations and transit times since last ventilation are consistent with the available sparse tracer data. This contrasts with OMP analysis, where a small number of end-members is fixed using traditional water mass analyses. Although the traditionally identified water mass ventilation regions (e.g., *Lazier* [1973], *Talley and McCartney* [1982], and *Pickart et al.* [2003] for Labrador Sea Water) and the most probable ventilation regions of the ME deconvolutions are in broad agreement, standard OMP analysis cannot quantify the uncertainty that comes from the fact that many alternatives are also consistent with the tracer data.

[81] 4. Ideal mean age has large entropic uncertainties with typical quartile error bars of ~50%. Away from the near-surface regions, where the boundary propagator has not decayed to zero by the end of the CFC period, ^{14}C is the only tracer that provides time information for $\tau \gtrsim 75$ a. While ^{14}C has nearly the ideal time dependence to constrain

the ideal mean age because of its slow radioactive decay, ^{14}C does not have the required spatially uniform boundary conditions to project perfectly onto the ideal mean age. Thus, even when the radiocarbon age is a good approximation to the ideal mean age, as is the case for the inversions with the AD prior plus CFCs, both radiocarbon and ideal mean age depend critically on the water mass fractions, that is, on the partitioning of a given water parcel according to where on the surface it was last ventilated. The large entropic uncertainties in the water mass fractions render both radiocarbon age and ideal mean age uncertain. It is worth emphasizing that even if a tracer had uniform boundary conditions and linear time dependence, only the first moment of the TTD would be well constrained; higher moments, and hence the shape of the TTD, would remain uncertain in the absence of additional constraints.

[82] 5. Transit time distributions of inverse Gaussian form whose two free parameters are determined by fitting anthropogenic transient tracers are not constrained by any data that contains information on long transit times. Such TTDs are appropriate for estimating the amount of anthropogenic carbon in the ocean [e.g., *Hall et al.*, 2002; *Terenzi et al.*, 2007; *Tanhua et al.*, 2009], which is propagated by the early ($\tau \lesssim 100$ a) part of the TTD. However, the mean age of such TTDs, as reported, for example, by *Tanhua et al.* [2009], can at best be considered a parameter of the inverse Gaussian, rather than a reliable estimate of the true mean transit time. The tails of these TTDs are determined by the assumed functional form, and the lack of data constraint in the tails likely renders their mean age highly uncertain. Furthermore, the assumption of a single dominant end-member, which motivates replacing the full surface origin–dependent boundary propagator with the TTD (a function of transit time only), introduces further uncertainty into both the ideal mean age and the anthropogenic carbon estimates from these TTDs, because the effect of surface variations in the boundary conditions is not taken into account.

[83] 6. The contributions of the uncertainties in the tracer data (interior and surface boundary conditions) to the uncertainties of the water mass fractions are modest and typically dominated by the entropic uncertainties. The greatest uncertainty thus comes from the underdetermined nature of the inversions: a broad multiplicity of possible solutions is consistent with what few data constraints are available. Interestingly, the data uncertainties not only broaden the entropic probability distribution but are also able to shift the most probable value. For the cases examined, such shifts fell within the range of the purely entropic error bars.

[84] Our study has shown to what degree the rich structure of the boundary propagator may be extracted from local bottle data, including repeat hydrography for CFC-11. Use of the ME method allowed the uncertainties associated with the limited information content of the available data (the entropic uncertainties) to be quantified. While those uncertainties are large per bottle, a great deal of the structure of the boundary propagator in the North Atlantic was revealed, with consistent patterns among the different inversion cases. The entropic uncertainties per bottle will be reduced when additional data constraints become available. Additional constraints will be provided by transient tracer species with boundary conditions and timescales different from the CFCs (e.g., ^{39}Ar) and by future repeat hydrographic surveys of transient tracer concentrations. Extensions of the method to incorporate information about the structure of tracer plumes and the geostropic balance of the flow are also likely to result in reduced entropic uncertainties. The uncertainties of volume averaged quantities will be reduced from the per-bottle uncertainties computed here, roughly by the inverse root of the number of statistically independent samples in the volume. We therefore expect that ventilation rate distributions [*Primeau and Holzer*, 2006], which require global volume integrals of $\mathcal{G}$, can be determined much more precisely than the local water mass fractions explored here.

Appendix A: Some Details of the Numerical Implementation

A1. Coarse Graining in Space and Time

[85] To reduce the computational burden we coarse grained the surface boundary conditions in both space and time. The 1° × 1° surface data was area averaged to 5° × 5° patches. Those 5° × 5° patches that overlapped the 1° × 1° land mask were used with a proportionately smaller area weight.

[86] The time history of the boundary conditions was coarse grained by sampling only at the following years: 0, 3, 6,…, 75, 80, 90, 120, 160, 200, 250, 300, 400,…, 1000, 1200, 1500, 2000,…, 4000, 5000, 7000, 9000, 11000, 15000, 20000 a. This provides adequate three yearly resolution of the CFC's time history to 75 years, after which the sampling becomes progressively coarser out to a cutoff time of 20000 a. In the case of the uniform prior, the prior itself was set to zero for transit times longer than 4000 a. Our results for water mass fractions older than a given threshold age (section 4.1) were insensitive to the cutoff time of the uniform prior as long as it was about 4000 a or longer. Sums of $\mathcal{P}$ over the year index n were evaluated in a way that is equivalent to interpolating $\mathcal{P}$ linearly between the sampled years and summing over all years.

A2. Solver Used

[87] The constraint equations (2) were solved numerically to high precision for the Lagrange multipliers with Matlab's *fsolve* routine which implements the Levenberg-Marquardt algorithm with line search and cubic interpolation. The analytic Jacobian $\partial\hat{C}_j/\partial\lambda_k$ was provided to *fsolve*.

A3. Data Restriction in the Case of No Solution

[88] Where no finite, high-precision solutions for the Lagrange multipliers could be found, the CFC-11 boundary conditions were nearly always inconsistent with the 1997 to 2003 change ΔF in the interior CFC-11 value. Such inconsistencies can for example result from eddy variability in the vicinity of large gradients. In the case of no solutions, the 1997 and 2003 CFC-11 measurements were averaged and assigned to either 1997 or 2003 depending on whether $\Delta F < 0$ or $\Delta F > 0$, respectively, while the CFC-11 value for the other year was ignored. This affected about 15% of the bottles for which both 1997 and 2003 CFC-11 concentrations were available. Removing CFC-11 for one of the years in this way almost always led to (finite, high-precision) solutions for the corresponding Lagrange multipliers.

However, it should be kept in mind that removing one time level of the CFC data restricts the ability of the inversions to shape the time dependence of the boundary propagator. Where results are presented for single profiles (e.g., Figure 8), we therefore selected profiles for which separate 1997 and 2003 CFC-11 measurements could be utilized for all bottles.

Appendix B: Gaussian Error Model

[89] In order to generate the synthetic data for our Monte Carlo uncertainty estimation, we built the following multivariate Gaussian error model. For the surface boundary conditions we use the standard deviation fields $\sigma(r)$ supplied with the WOA05 and GLODAP data sets to estimate the spatial autocovariance as $\sigma^2(r)$. Terms that happened to be zero (no uncertainty) were replaced by the minimum nonzero value of $\sigma^2(r)$. The off-diagonal elements of the spatial covariance were assumed to decay exponentially with geodesic distance over a decorrelation scale of 500 km. More precisely, the covariance between surface points r_i and r_j, separated by geodesic distance d_{ij} was specified as $\sigma(r_i)\sigma(r_j)\exp(-d_{ij}/L)$, with L = 500 km. The value of 500 km is somewhat arbitrary, but to err on the side of overestimating the effect of the spatial correlations we chose L to be about ten midlatitude Rossby deformation radii. The true length scale is likely much shorter especially across frontal regions. The standard error estimates of the GLODAP data were extended from their edges first zonally and then toward the poles to fill in the missing regions. More careful interpolation was not deemed necessary for the purpose of error estimation.

[90] In principle, synthetic error fields should also have some temporal covariance to statistically model the memory of the mixed layer, but it is difficult to account for this given our nonuniformly spaced sample times and lack of a detailed analysis of the temporal correlations. Such an analysis from available data or climate models is certainly beyond the scope of this paper. We therefore simply treat every month of each of the sample years as statistically independent. This amounts to a random perturbation of the seasonal cycle for each sample year, with the nonuniform spacing of the years effectively building in some memory. Note that because of the coarse temporal sampling at long times, we conservatively overestimate the effect of errors in the tails of the distribution. (In a convolution such errors would tend to average out.)

[91] To generate the multivariate Gaussian synthetic error field of the boundary conditions with the specified spatial covariance structure, the spatial covariance matrix was Cholesky factorized and the resulting lower triangular matrix multiplied by a vector of unit variance, independent Gaussian random numbers, independently for every month of each sample year in our coarse-grained time history.

[92] The variance of the interior data was estimated as follows. For the assumed cyclostationary tracers of θ, S, and PO_4^*, the variance was simply computed from the 1997 and 2003 values of the line A20 repeat hydrographies. To estimate the temporal variance of the CFC-11 data at a specified depth, we examined data from line W, which was sampled almost every year (sometimes twice a year) from 1994 to 2008. The profiles of line W data were interpolated to the depth of interest and the variance of CFC-11 concentration was computed from all measurements that were taken within one degree of latitude of the location of interest over the 1994–2008 period, after a linear trend was subtracted out. At ~40°N between 1 and 2 km depth, the corresponding standard deviation ranged from 9% to 15% of the 2003 concentrations. To be conservative, we used a standard deviation of 15% for the interior data.

[93] A member of the data ensemble used for a given bottle thus corresponds to (1) the boundary conditions plus synthetic errors of the desired covariance added independently for each year and month of our coarsely sampled time history and (2) the bottle tracer data plus random Gaussian errors for each tracer field with the desired variance. Covariances between the different tracer species were neglected for both surface and interior data.

Appendix C: AD Prior

[94] The surface patches that were used to compute the coarse-grained Green functions of the AD prior (equation (11)) are shown in Figure C1. For comparison with Figure 8, we show in Figure C2a the corresponding profiles of the distributions of times since last surface contact anywhere as obtained from the AD prior alone, without any tracer constraints. Figure C2b shows the AD prior's ideal mean age for comparison with Figure 9.

Appendix D: Relationship Between Radiocarbon Age and Ideal Mean Age

[95] We derive the relationship between radiocarbon age and ideal mean age for the realistic case of spatially inhomogeneous radiocarbon concentrations. This generalizes the single-end-member case discussed by, e.g., *Deleersnijder et al.* [2001], *Hall et al.* [2002], and *Waugh et al.* [2003], and allows us to see how the entropic uncertainties of ideal mean age manifest themselves for radiocarbon age. For simplicity of exposition, we use discrete surface index s, but continuous transit time τ.

[96] The true ideal mean age $\Gamma(\mathbf{r})$ is defined by

$$\Gamma(\mathbf{r}) = \sum_s \int_0^\infty d\tau\, \tau\, \mathcal{G}(\mathbf{r}|s,\tau), \tag{D1}$$

while the radiocarbon age $\Gamma_C(\mathbf{r})$ is defined in terms of the radiocarbon concentration $C(\mathbf{r})$ by

$$C(\mathbf{r}) = e^{-\gamma\Gamma_C(\mathbf{r})} C_0(\mathbf{r}), \tag{D2}$$

where the initial concentration $C_0(\mathbf{r})$ is given by

$$C_0(\mathbf{r}) \equiv \sum_s f(s|\mathbf{r}) C(s), \tag{D3}$$

with $f(s|\mathbf{r}) \equiv \int_0^\infty d\tau \mathcal{G}(\mathbf{r}|s,\tau)$ being the water mass fractions regardless of transit time (in terms of equation (12), $f(s|\mathbf{r}) \equiv f(s, 0|\mathbf{r}, m_0)$).

[97] The relationship between Γ_C and Γ can be seen by expressing $C(\mathbf{r})$ in terms of the propagated surface concentrations $C(s)$ as

$$C(\mathbf{r}) = \sum_s \int_0^\infty d\tau\, \mathcal{G}(\mathbf{r}|s,\tau) e^{-\gamma\tau} C(s), \tag{D4}$$

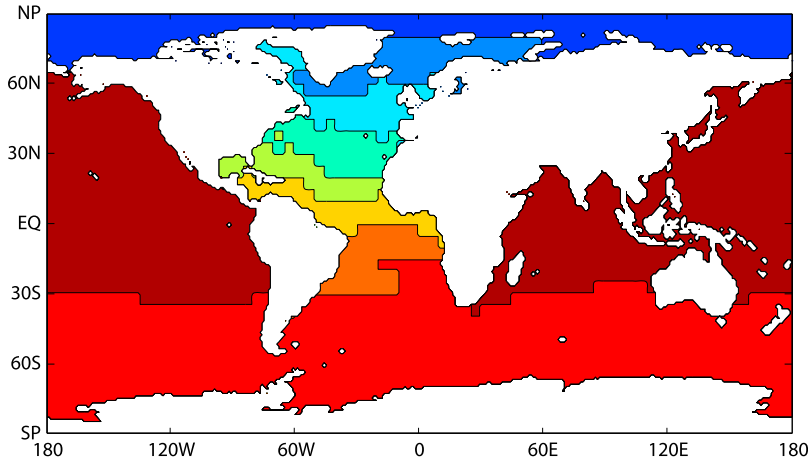

Figure C1. The set of nine surface patches, Ω_i, based on annual average density contours, used to compute the patch-integrated boundary propagator of a steady advective-diffusive transport operator [*Primeau*, 2005]. The AD prior was constructed from this boundary propagator as described in section 2.2 and Appendix C.

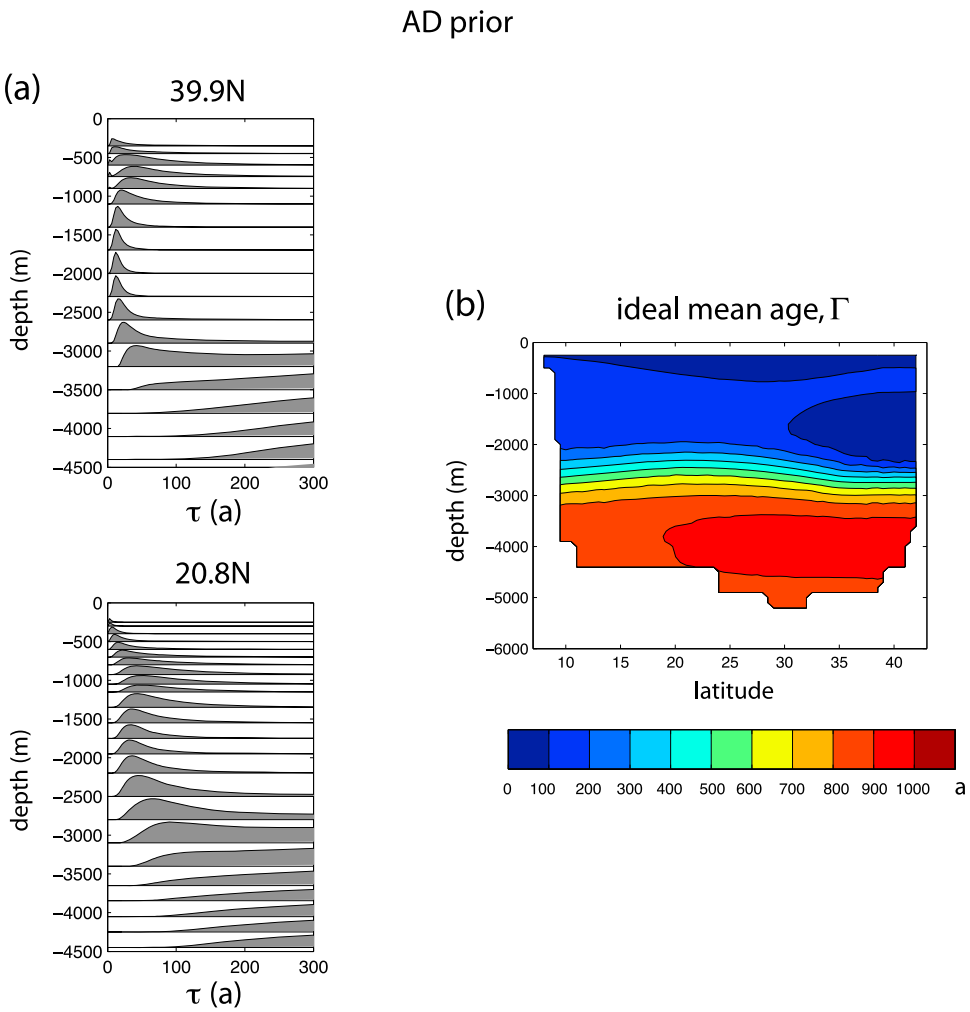

Figure C2. (a) The AD prior's seasonally averaged distribution of times since last contact with the surface anywhere for the A20 profiles indicated. For plotting, the distributions have been normalized by their maximum value and scaled to fit the space between adjacent depths. (b) The AD prior's ideal mean age (mean time since last surface contact) for section A20.

which is equation (1) for steady flow. Expanding $e^{-\gamma\tau}$ to second order in γ about $\tau = \Gamma(\mathbf{r})$, (D4) can be rewritten as

$$C(\mathbf{r}) = e^{-\gamma\Gamma(\mathbf{r})}C_0(\mathbf{r})\left(1 - \gamma\sum_s \delta\hat{C}(s)\delta\Gamma(s,\mathbf{r}) + \gamma^2\Delta^2(\mathbf{r})\frac{\overline{C}}{C_0(\mathbf{r})} + \gamma^2\sum_s \delta\hat{C}(s)D^2(s,\mathbf{r})\right), \quad \text{(D5)}$$

with the following definitions:

$$\delta C(s) \equiv C(s) - \overline{C}, \quad \text{(D6)}$$

where $\overline{C}$ is the spatial area average of $C(s)$, and

$$\delta\hat{C}(s,\mathbf{r}) \equiv \delta C(s)/C_0(\mathbf{r}), \quad \text{(D7)}$$

$$\delta\Gamma(s,\mathbf{r}) \equiv \int_0^\infty d\tau\, \mathcal{G}(\mathbf{r}|s,\tau)(\tau - \Gamma(\mathbf{r})), \quad \text{(D8)}$$

$$2D^2(s,\mathbf{r}) \equiv \int_0^\infty d\tau\, \mathcal{G}(\mathbf{r}|s,\tau)(\tau - \Gamma(\mathbf{r}))^2. \quad \text{(D9)}$$

Equation (D5) is valid provided order γ^3 terms are negligible. Note that $\sum_s \delta\Gamma(s, \mathbf{r}) = 0$ and $\sum_s D^2(s, \mathbf{r}) = \Delta^2(\mathbf{r})$, where $\Delta(\mathbf{r})$ is the width of the TTD defined by $2\Delta^2(\mathbf{r}) = \sum_s \int_0^\infty d\tau \mathcal{G}(\mathbf{r}|s, \tau)\,(\tau - \Gamma(\mathbf{r}))^2$. The terms of (D5) involving $\delta\hat{C}(s, \mathbf{r})$ are due to spatial inhomogeneity of the ^{14}C surface concentration.

[98] For ^{14}C the spatial variations $\delta C(s)$ are small compared to the actual concentration $C_0(\mathbf{r})$ so that the $\delta\hat{C}(s, \mathbf{r})$ are expected to be small. How small the order γ and γ^2 sums over surface index s in (D5) are depends on the detailed form of the boundary propagator through $\delta\Gamma(s, \mathbf{r})$ and $D(s, \mathbf{r})$. Throughout the Atlantic the width Δ is expected to be small compared to the decay timescale, because Δ and Γ are typically of the same order of magnitude, and $1/\gamma \sim 8300$ a. For the inversions with the uniform prior, the maximum of $\gamma\Delta \sim 0.03$. For the inversions with the AD prior, $\gamma\Delta$ can reach as high as 0.1 near the surface and in the middepth CFC plume because of the subtly overweighted tails of the TTDs there (see section 5.3), but below ~3000 m $\gamma \lesssim 0.03$. Thus, the term $\sim\gamma^2\Delta^2$ in (D5) can be neglected to a good approximation for section A20, as expected. If in addition the order γ and γ^2 terms involving $\delta\hat{C}$ are small compared to unity we have

$$C(\mathbf{r}) \simeq e^{-\gamma\Gamma(\mathbf{r})}C_0(\mathbf{r}), \quad \text{(D10)}$$

so that $\Gamma_C(\mathbf{r}) \simeq \Gamma(\mathbf{r})$.

[99] Note that the spatial variations in the surface ^{14}C concentration are critical in determining the initial radiocarbon concentration $C_0(\mathbf{r})$ via the water mass fractions from equation (D3). The large entropic uncertainties in the water mass fractions $f(s|\mathbf{r})$ propagate by way of equation (D3) into the initial radiocarbon concentration $C_0(\mathbf{r})$ and into the radiocarbon age, $\Gamma_C(\mathbf{r}) = \gamma^{-1}\log[C_0(\mathbf{r})/C(\mathbf{r})]$. Thus, the entropic uncertainties in the water mass fractions only come into play when the ^{14}C boundary conditions vary spatially. If the surface ^{14}C concentration was uniform, the entropic uncertainty in the water mass fractions would have no effect on the uncertainty of the radiocarbon age, and because $\Gamma_C \simeq \Gamma$ in that case, our estimate of the uncertainties of the ideal mean age would be much lower.

[100] **Acknowledgments.** This work was supported by NSF grants OCE-0727229 (Columbia) and OCE-0726871 (UC Irvine). We thank Tim Hall for discussions and Hoyle Lee for providing CFC data for line W and CFC saturation data for the North Atlantic. We are grateful to Rolf Sonnerup and two anonymous referees for providing valuable comments that led to an improved manuscript.

References

Anderson, L. A., and J. L. Sarmiento (1994), Redfield ratios of remineralization determined by nutrient data analysis, *Global Biogeochem. Cycles*, *8*, 65–80.

Antonov, J. I., R. A. Locarnini, T. P. Boyer, A. V. Mishonov, and H. E. Garcia (2006), *World Ocean Atlas 2005*, vol. 2, *Salinity*, *NOAA Atlas NESDIS*, vol. 62, edited by S. Levitus, 182 pp., NOAA, Silver Spring, Md.

Bower, A. S., and H. D. Hunt (2000), Lagrangian observations of the Deep Western Boundary Current in the North Atlantic Ocean. Part I: Large-scale pathways and spreading rates, *J. Phys. Oceanogr.*, *30*, 764–783.

Broecker, W. S., and T.-H. Peng (2000), Comparison of ^{39}Ar and ^{14}C ages for waters in the deep ocean, *Nucl. Instrum. Methods Phys. Res., Sect. B*, *172*, 473–478.

Broecker, W. S., et al. (1998), How much deep water is formed in the Southern Ocean?, *J. Geophys. Res.*, *103*, 15,833–15,843.

de Brauwere, A., S. H. M. Jacquet, F. De Ridder, F. Dehairs, R. Pintelon, J. Schoukens, and W. Baeyens (2007), Water mass distributions in the Southern Ocean derived from a parametric analysis of mixing water masses, *J. Geophys. Res.*, *112*, C02021, doi:10.1029/2006JC003742.

Deleersnijder, E., J.-M. Campin, and E. Delhez (2001), The concept of age in marine modelling: I. Theory and preliminary model results, *J. Mar. Syst.*, *28*, 229–267.

Dickson, R. R., and J. Brown (1994), The production of North Atlantic Deep Water: Sources, rates and pathways, *J. Geophys. Res.*, *99*, 12,319–12,341.

Dickson, R. R., E. Gmitrowicz, and A. Watson (1990), Deep water renewal in the northern North Atlantic, *Nature*, *344*, 848–850.

Doney, S., and W. Jenkins (1994), Ventilation of the Deep Western Boundary Current and abyssal western North Atlantic: Estimates from tritium and ^{3}He distributions, *J. Phys. Oceanogr.*, *24*, 638–659.

Garcia, H. E., R. A. Locarnini, T. P. Boyer, and J. I. Antonov (2006a), *World Ocean Atlas 2005*, vol. 3, *Dissolved Oxygen, Apparent Oxygen Utilization, and Oxygen Saturation*, *NOAA Atlas NESDIS*, vol. 63, edited by S. Levitus, 342 pp., NOAA, Silver Spring, Md.

Garcia, H. E., R. A. Locarnini, T. P. Boyer, and J. I. Antonov (2006b), *World Ocean Atlas 2005*, vol. 4, *Nutrients (Phosphate, Nitrate, and Silicate), NOAA Atlas NESDIS*, vol. 64, edited by S. Levitus, 396 pp., NOAA, Silver Spring, Md.

Gent, P. R., and J. C. McWilliams (1990), Isopycnal mixing in ocean circulation models, *J. Phys. Oceanogr.*, *20*, 150–155.

Girton, J. B., T. B. Sanford, and R. H. Käse (2001), Synoptic sections of the Denmark Strait overflow, *Geophys. Res. Lett.*, *28*, 1619–1622.

Gull, S. F., and G. J. Daniell (1978), Image reconstruction from incomplete and noisy data, *Nature*, *272*, 686–690.

Haine, T. W. N., and T. M. Hall (2002), A generalized transport theory: Water-mass composition and age, *J. Phys. Oceanogr.*, *32*, 1932–1946.

Haine, T. W. N., and K. J. Richards (1995), The influence of the seasonal mixed layer on oceanic uptake of CFCs, *J. Geophys. Res.*, *100*, 10,727–10,744.

Hall, M. M., T. M. Joyce, R. S. Pickart, W. M. Smethie Jr., and D. J. Torres (2004), Zonal circulation across 52°W in the North Atlantic, *J. Geophys. Res.*, *109*, C11008, doi:10.1029/2003JC002103.

Hall, T. M., T. W. N. Haine, and D. W. Waugh (2002), Inferring the concentration of anthropogenic carbon in the ocean from tracers, *Global Biogeochem. Cycles*, *16*(4), 1131, doi:10.1029/2001GB001835.

Hall, T. M., T. W. N. Haine, M. Holzer, D. A. LeBel, F. Terenzi, and D. W. Waugh (2007), Ventilation rates estimated from tracers in the presence of mixing, *J. Phys. Oceanogr.*, *37*, 2599–2611.

Hansen, B., and S. Osterhus (2007), Faroe Bank Channel overflow 1995–2005, *Prog. Oceanogr.*, *75*, 817–856.

Harvey, J. G., and A. Theodorou (1986), The circulation of Norwegian Sea overflow water in the eastern North Atlantic, *Oceanol. Acta*, *9*, 393–402.

Hogg, N., R. Pickart, R. Hendry, and W. Smethie (1986), On the northern recirculation gyre of the Gulf Stream, *Deep Sea Res., Part A*, *33*, 1139–1165.

Holzer, M., and T. M. Hall (2000), Transit-time and tracer-age distributions in geophysical flows, *J. Atmos. Sci.*, *57*, 3539–3558.
Holzer, M., and F. W. Primeau (2006), The diffusive ocean conveyor, *Geophys. Res. Lett.*, *33*, L14618, doi:10.1029/2006GL026232.
Holzer, M., and F. W. Primeau (2008), The path-density distribution of oceanic surface-to-surface transport, *J. Geophys. Res.*, *113*, C01018, doi:10.1029/2006JC003976.
Huhn, O., W. Roether, and R. Steinfeldt (2008), Age spectra in North Atlantic Deep Water along the South American continental slope, 10°N–30°S, based on tracer observations, *Deep Sea Res., Part I*, *55*, 1252–1276.
Jaynes, E. T. (1957), Information theory and statistical mechanics, *Phys. Rev.*, *106*, 620–630.
Jenkins, W. J., and P. Rhines (1980), Tritium in the deep North Atlantic Ocean, *Nature*, *286*, 877–880.
Key, R. M., A. Kozyr, C. L. Sabine, K. Lee, R. Wanninkhof, J. L. Bullister, R. A. Feely, F. J. Millero, C. Mordy, and T.-H. Peng (2004), A global ocean carbon climatology: Results from Global Data Analysis Project (GLODAP), *Global Biogeochem. Cycles*, *18*, GB4031, doi:10.1029/2004GB002247.
Khatiwala, S., M. Visbeck, and P. Schlosser (2001), Age tracers in an ocean GCM, *Deep Sea Res., Part I*, *48*, 1423–1441.
Khatiwala, S., F. W. Primeau, and T. M. Hall (2009), Reconstruction of the history of anthropogenic CO_2 concentrations in the ocean, *Nature*, *462*, 346–349.
Kibler, S., and F. Primeau (2006), A maximum entropy approach to water mass analysis, *Eos Trans. AGU*, *87*(52), Fall Meet. Suppl., Abstract OS41A-0572.
Large, W. G., J. C. McWilliams, and S. C. Doney (1994), Oceanic vertical mixing: A review and a model with a nonlocal boundary layer parameterization, *Rev. Geophys.*, *32*, 363–403.
Lazier, J. (1973), The renewal of Labrador Sea water, *Deep Sea Res. Oceanogr. Abstr.*, *20*, 341–353.
LeBel, D. A., et al. (2008), The formation rate of North Atlantic Deep Water and eighteen degree water calculated from CFC-11 inventories observed during WOCE, *Deep Sea Res., Part I*, *55*, 891–910.
Lilly, J. M., P. B. Rhines, M. Visbeck, R. Davis, J. R. N. Lazier, F. Schott, and D. Farmer (1999), Observing deep convection in the Labrador Sea during winter 1994/95, *J. Phys. Oceanogr.*, *29*, 2065–2098.
Locarnini, R. A., A. V. Mishonov, J. I. Antonov, T. P. Boyer, and H. E. Garcia (2006), *World Ocean Atlas 2005*, vol. 1, *Temperature*, NOAA Atlas NESDIS, vol. 61, edited by S. Levitus, 182 pp., NOAA, Silver Spring, Md.
Mauritzen, C. (1996), Production of dense overflow waters feeding the North Atlantic across the Greenland-Scotland Ridge. Part 1: Evidence for a revised circulation scheme, *Deep Sea Res., Part 1*, *43*, 769–806.
Meincke, J. (1983), The modern current regime across the Greenland-Scotland Ridge, in *Structure and Development of the Greenland-Scotland Ridge*, edited by M. Bott et al.., pp. 637–650, Plenum, New York.
Östlund, H. G., and C. G. H. Rooth (1990), The North Atlantic tritium and radiocarbon transients 1972–1983, *J. Geophys. Res.*, *95*, 20,147–20,165.
Pacanowski, R. C., K. Dixon, and A. Rosati (1993), The GFDL modular ocean model users guide, *Tech. Rep. 2*, Ocean Group, Geophys. Fluid Dyn. Lab., Princeton, N. J.
Peacock, S., and M. Maltrud (2006), Transit-time distributions in a global ocean model, *J. Phys. Oceanogr.*, *36*, 474–495.
Pickart, R. S., and W. M. Smethie (1998), Temporal evolution of the deep western boundary current where it enters the sub-tropical domain, *Deep Sea Res., Part I*, *45*, 1053–1083.
Pickart, R. S., W. Smethie, J. Lazier, E. Jones, and W. Jenkins (1996), Eddies of newly-formed upper Labrador Sea water, *J. Geophys. Res.*, *101*, 20,711–20,726.
Pickart, R. S., F. Straneo, and G. W. K. Moore (2003), Is Labrador Sea water formed in the Irminger basin?, *Deep Sea Res., Part I*, *50*, 23–52.
Press, W. H., S. A. Teukolsky, W. T. Vetterling, and B. P. Flannery (2007), *Numerical Recipes: The Art of Scientific Computing*, 3rd ed., Cambridge Univ. Press, Cambridge, U. K.
Primeau, F. W. (2005), Characterizing transport between the surface mixed layer and the ocean interior with a forward and adjoint global ocean transport model, *J. Phys. Oceanogr.*, *35*, 545–564.
Primeau, F. W., and M. Holzer (2006), The ocean's memory of the atmosphere: Residence-time and ventilation-rate distributions of water masses, *J. Phys. Oceanogr.*, *36*, 1439–1456.
Primeau, F. W., and S. Kibler (2008), How much water forms in the Southern Ocean? A maximum entropy approach to global water mass analysis, *Eos Trans. AGU*, *89*(53), Fall Meet. Suppl., Abstract H21B-0817.
Rhein, M., L. Stramma, and U. Send (1995), The Atlantic Deep Western Boundary Current: Water masses and transports near the equator, *J. Geophys. Res.*, *100*, 2441–2457.
Ross, C. K. (1984), Temperature-salinity characteristics of the "overflow" water in Denmark Strait during OVERFLOW 73, *Rapp. P. V. Reun. Cons. Int. Explor. Mer.*, *185*, 111–119.
Rudels, B., E. Fahrbach, J. Meincke, G. Budeus, and P. Eriksson (2002), The East Greenland Current and its contribution to the Denmark Strait overflow, *ICES J. Mar. Sci.*, *59*, 1133–1154.
Sabine, C. L., R. M. Key, A. Kozyr, R. A. Feely, R. Wanninkhof, F. J. Millero, T.-H. Peng, J. L. Bullister, and K. Lee (2005), Global Ocean Data Analysis Project (GLODAP): Results and data, *ORNL/CDIAC-145*, 110 pp., Carbon Dioxide Inf. Anal. Cent., Oak Ridge Natl. Lab., U.S. Dep. of Energy, Oak Ridge, Tenn.
Sarmiento, J. L., N. Gruber, M. A. Brzezinski, and J. P. Dunne (2004), High-latitude controls of thermocline nutrients and low latitude biological productivity, *Nature*, *427*, 56–60.
Saunders, P. (1990), Cold outflow from the Faroe Bank Channel, *J. Phys. Oceanogr.*, *20*, 29–43.
Schmitz, W., and M. McCartney (1993), On the North Atlantic circulation, *Rev. Geophys.*, *31*, 29–49.
Shannon, C. E. (1951), Prediction and entropy of printed English, *Bell Syst. Tech. J.*, *30*, 50–64.
Skilling, J., and S. F. Gull (1991), Bayesian maximum entropy image reconstruction, in *Spatial Statistics and Imaging: Papers From the Research Conference on Image Analysis and Spatial Statistics Held at Bowdoin College, Brunswick, Maine, Summer 1988*, edited by A. Possolo, pp. 341–367, Inst. of Math. Stat., Hayward, Calif.
Smethie, W. M., Jr. (1993), Tracing the thermohaline circulation in the western North Atlantic using chlorofluorocarbons, *Prog. Oceanogr.*, *31*, 51–99.
Smethie, W. M., Jr., and R. A. Fine (2001), Rates of North Atlantic Deep Water formation calculated from chlorofluorocarbon inventories, *Deep Sea Res., Part I*, *48*, 189–215.
Smethie, W. M., Jr., R. A. Fine, A. Putzka, and E. P. Jones (2000), Tracing the flow of North Atlantic Deep Water using chlorofluorocarbons, *J. Geophys. Res.*, *105*, 14,297–14,323.
Smethie, W. M., Jr., D. A. LeBel, R. A. Fine, M. Rhein, and D. Kieke (2007), Strength and variability of the deep limb of the North Atlantic Meridional Circulation from chlorofluorocarbon inventories, in *Ocean Circulation: Mechanisms and Impacts—Past and Future Changes of the Meridional Overturning Circulation*, *Geophys. Monogr. Ser.*, vol. 173, edited by A. Schmittner, J. Chiang, and S. Hemmings, pp. 119–130, AGU, Washington, D. C.
Steinfeldt, R., and M. Rhein (2004), Spreading velocities and dilution of North Atlantic Deep Water in the tropical Atlantic based on CFC time series, *J. Geophys. Res.*, *109*, C03046, doi:10.1029/2003JC002050.
Steinfeldt, R., M. Rhein, and M. Walter (2007), NADW transformation at the western boundary between 66°W/20°N and 60°W/10°N, *Deep Sea Res., Part I*, *54*, 835–855.
Stommel, H. (1979), Determination of watermass properties of water pumped down from the Ekman layer to the geostropic flow below, *Proc. Natl. Acad. Sci. U. S. A.*, *76*, 3051–3055.
Stramma, L., D. Kieke, M. Rhein, F. Schott, I. Yashayaev, and K. Koltermann (2004), Deep water changes at the western boundary of the subpolar North Atlantic during 1996 to 2001, *Deep Sea Res., Part I*, *51*, 1033–1056.
Swift, J. H. (1984), The circulation of the Denmark Strait and Iceland-Scotland overflow waters in the North Atlantic, *Deep Sea Res., Part A*, *31*, 1339–1355.
Swift, J. H., K. Aagaard, and S.-A. Malmberg (1980), The contribution of the Denmark Strait overflow to the deep North Atlantic, *Deep Sea Res., Part A*, *27*, 29–42.
Talley, L., and M. McCartney (1982), Distribution and circulation of Labrador Sea water, *J. Phys. Oceanogr.*, *12*, 1189–1205.
Tanhua, T., K. Olsson, and E. Jeansson (2005), Formation of Denmark Strait overflow water and its hydro-chemical composition, *J. Mar. Syst.*, *57*, 264–268.
Tanhua, T., E. P. Jones, E. Jeansson, S. Jutterström, W. M. Smethie Jr., D. W. R. Wallace, and L. G. Anderson (2009), Ventilation of the Arctic Ocean: Mean ages and inventories of anthropogenic CO_2 and CFC-11, *J. Geophys. Res.*, *114*, C01002, doi:10.1029/2008JC004868.
Terenzi, F., T. M. Hall, S. Khatiwala, C. B. Rodehacke, and D. A. LeBel (2007), Uptake of natural and anthropogenic carbon by the Labrador Sea, *Geophys. Res. Lett.*, *34*, L06608, doi:10.1029/2006GL028543.
Tomczak, M. (1981), A multiparameter extension of temperature/salinity diagram techniques for the analysis of non-isopycnal mixing, *Prog. Oceanogr.*, *10*, 147–171.
Tomczak, M., and D. G. Large (1989), Optimum multiparameter analysis of mixing in the thermocline of the eastern Indian Ocean, *J. Geophys. Res.*, *94*, 16,141–16,149.

Walker, S. J., R. F. Weiss, and P. K. Salameh (2000), Reconstructed histories of the annual mean atmospheric mole fractions for the halocarbons CFC-11, CFC-12, CFC-113, and carbon tetrachloride, *J. Geophys. Res.*, *105*, 14,285–14,296.

Warner, M. J., and R. F. Weiss (1985), Solubilities of chlorofluorocarbons 11 and 12 in water and seawater, *Deep Sea Res., Part. A*, *32*, 1485–1497.

Watts, D. (1991), Equatorward currents in temperatures 1.8–6.0°C on the continental slope in the Mid-Atlantic Bight, in *Deep Convection and Deep Water Formation in the Oceans*, edited by P. C. Chu and J. C. Gascard, pp. 183–196, Elsevier, Amsterdam.

Waugh, D. W., T. M. Hall, and T. W. N. Haine (2003), Relationships among tracer ages, *J. Geophys. Res.*, *108*(C5), 3138, doi:10.1029/2002JC001325.

Waugh, D. W., T. W. N. Haine, and T. M. Hall (2004), Transport times and anthropogenic carbon in the subpolar North Atlantic Ocean, *Deep Sea Res., Part I*, *51*, 1475–1491.

Weiss, R., J. Bullister, R. Gammon, and M. Warner (1985), Atmospheric chlorofluoromethanes in the deep equatorial Atlantic, *Nature*, *314*, 608–610.

Williams, R. G., J. C. Marshall, and M. A. Spall (1995), Does Stommel's mixed layer "demon" work?, *J. Phys. Oceanogr.*, *25*, 3089–3102.

Williams, R. G., V. Roussenov, and M. J. Follows (2006), Nutrient streams and their induction into the mixed layer, *Global Biogeochem. Cycles*, *20*, GB1016, doi:10.1029/2005GB002586.

M. Holzer, School of Mathematics and Statistics, University of New South Wales, Sydney, NSW 2052, Australia. (hm2220@columbia.edu)

S. Khatiwala and W. M. Smethie Jr., Lamont-Doherty Earth Observatory, Earth Institute at Columbia University, Palisades, NY 10964, USA. (spk@ldeo.columbia.edu; bsmeth@ldeo.columbia.edu)

F. W. Primeau, Department of Earth System Science, University of California, 3216 Croul Hall, Irvine, CA 92697-3100, USA. (fprimeau@uci.edu)